Langmuir Turbulence in the Arctic Ocean: Insights From a Coupled Sea Ice –Wave Model

Aikaterini Tavri[1], Chris Horvat[1], Brodie Pearson[2], Guillaume Boutin[3], Anne Hansen[2], and Ara Lee[2]
[1]Brown University, Providence, RI, USA
[2]Oregon State University, Corvallis, OR, USA
[3]Nansen Environmental and Remote Sensing Center and Bjerknes Centre for Climate Research, Bergen, Norway
Correspondence: Aikaterini Tavri `aikaterini_tavri@brown.edu`

Abstract. Upper-ocean mixing regulates the vertical transport of heat, momentum, and tracers in the ocean surface boundary layer~~, yet its representation under sea ice remains highly uncertain~~. Langmuir turbulence (LT), generated by the interaction of wind stress and wave-induced Stokes drift, is a dominant ~~open-ocean mixing mechanism and has been observed in~~ mixing mechanism in the open ocean. Observations of LT in leads, polynyas, and the marginal ice zone (MIZ) confirm its presence in ice-covered regions, but its Arctic-wide occurrence and modulation by sea ice and waves ~~are poorly constrained~~remain limited in characterization. Here we present the first pan-Arctic assessment of LT mixing potential using a ~~fully coupled sea ice–wave modeling framework~~ coupled sea ice–wave model integrating *neXtSIM* and *WAVEWATCH III*. ~~Combining wind–wave forcing metricswith mixed-layer–integrated dissipation and vertical kinetic energy diagnostics~~Using wind–wave forcing metrics, we show that LT-relevant forcing beneath sea ice is spatially confined and ~~strongly~~ highly intermittent. Conditions ~~capable of sustaining LT occur primarily~~ favorable for LT largely occur within the seasonal MIZ and arise episodically~~during late melt and freeze-up, rather than as a persistent background state~~. Sea ice concentration ~~regulates~~ sets the mean balance between wave- and shear-driven turbulence, ~~while ice mechanical state, wave properties, and wind–wave misalignment control the efficiency of Langmuir-driven vertical motions without altering the underlying mixing regimes~~but does not uniquely determine LT variability. The realization of wave-driven mixing depends on wave conditions and ice structure, while wind–wave misalignment plays a secondary role. As a result, LT in the Arctic MIZ ~~most often coexists with wind-driven shear in~~ typically occurs within mixed-forcing regimes, ~~highlighting the need for regime-aware representations of~~ where wave-driven and shear-driven processes coexist. Our findings highlight the importance of wave–ice interactions and intermittency in shaping upper-ocean mixing ~~in climate models.~~ under partial ice cover.

1 Introduction

The Arctic Ocean has traditionally been considered a region of weak upper-ocean mixing, primarily due to extensive sea ice cover that insulates the ocean from atmospheric forcing and dissipates wave energy (Morison et al., 1985; Pinkel, 2005). Under these conditions, turbulent exchange in the ocean surface boundary layer (OSBL) remains strongly suppressed, and vertical mixing occurs only during sporadic shear-driven and convective events. In recent decades, the rapid decline in the Arctic sea ice, marked by the loss of multiyear ice, earlier seasonal melt onset, and expansion of open water area, has increasingly exposed the Arctic Ocean to wind and wave forcing, fundamentally shifting the traditional view (Stopa et al., 2016; Armitage et al., 2017; Muilwijk et al., 2024). These changes have amplified air–sea momentum transfer (Rainville et al., 2011; Dosser and Rainville, 2016) and expanded the Marginal Ice Zone (MIZ), a transitional region characterized by discontinuous ice cover that enables surface wave propagation and interaction with the floe field (Collins et al., 2018; Boutin et al., 2020).

Within the MIZ, surface gravity waves play a central role in mediating air–sea interaction. They modulate sea ice breakup and accelerate melt through enhanced mechanical stress and turbulent mixing (Thomson and Rogers, 2014; Thomson, 2022). Beyond direct wave breaking, surface waves also ~~generate~~ enhance upper-ocean turbulence through Langmuir turbulence (LT), that develops when wind-forced shear aligns with wave-induced Stokes drift (Craik and Leibovich, 1976; Leibovich, 1983; McWilliams et al., 1997). LT forms coherent, counter-rotating Langmuir cells that vertically redistribute heat, momentum, and tracers, (Skyllingstad and Denbo, 1995; Kukulka et al., 2013; D'Asaro, 2014; Gargett and Grosch, 2014), and it has emerged as a key regulator of mixed layer dynamics in the open ocean ~~(Belcher et al., 2012; Yang et al., 2014). The absence of LT parameterizations in~~ (Polton and Belcher, 2007; Belcher et al., 2012; Yang et al., 2014; Pearson et al., 2015). *In situ* observations show that waves can propagate long distances beneath sea ice and influence mixing near leads, polynyas, and the MIZ (Drucker et al., 2003; Kirillov et al., 2013; Horvat et al., 2020; Cooper et al., 2022). The presence of Langmuir cells in ice openings further confirms that LT remains active in ice-covered waters, albeit intermittently and with modified structure (Dethleff and Kempema, 200 . Prior studies of wave–ice interactions have largely focused on mechanical processes such as ice breakup and wave attenuation (Collins et al., 2018; Squire, 2018), while the role of LT in modulating turbulent mixing under sea ice remains understudied.

Experiments using ocean general circulation models~~contributes~~ , show that neglecting LT leads to systematic biases in upper-ocean structure, including underestimation of summer mixed layer depth ~~and~~ (MLD) and misrepresentation of seasonal stratification (Li et al., 2019). Incorporating LT reduces these biases and improves simulations of sea surface temperature ~~, particularly in wind- and wave-active regions such as the Southern Ocean (Belcher et al., 2012; Li et al., 2019).~~

~~Large eddy~~ and ocean heat content (Fan and Griffies, 2014; Ali et al., 2019). Additionally, Large-eddy simulation (LES) studies ~~show that LT deepens~~ have demonstrated that LT substantially enhances upper-ocean mixing, deepening the mixed layer and ~~enhances~~ increasing vertical entrainment fluxes by up to an order of magnitude ~~compared~~ relative to shear-driven turbulence alone, ~~while also moderately increasing~~ with more moderate increases in momentum fluxes (McWilliams et al., 1997; Sullivan et al., 2007). ~~Enhanced vertical mixing leads to elevated turbulent kinetic energy (TKE) and stronger entrainment across density interfaces (Polton and Belcher, 2007; Pearson et al., 2015; Ali et al., 2019). These insights have motivated the development of new LT parameterizations for~~ Therefore, representing open-ocean LT in large-scale ~~models that incorporate wave–current interactions and Stokes production terms (Van Roekel et al., 2012; Harcourt, 2015; Li and Fox-Kemper, 2017). Despite these advances, existing~~ models is essential, as it leads to significant regional and global climate impacts (Li et al., 2016, 2017). Typically, LT parameterizations are incorporated into ocean models through modifications to turbulence closure schemes such as the K-profile parameterization (KPP) (Li and Fox-Kemper, 2017), enhancing upper-ocean mixing by increasing turbulent velocity scales and promoting entrainment at the base of the mixed layer (Van Roekel et al., 2012; Harcourt, 2015; Reichl et al., 2016; Li an . These improve the representation of upper ocean physics but differ in their ability to represent LT across dynamical regimes, highlighting uncertainties in their formulation and performance (Li et al., 2019; Ali et al., 2019).

Despite the demonstrated importance of LT in the open ocean, these parameterizations have not been systematically evaluated in ~~sea~~ ice-covered regions, where the physical environment deviates substantially from typical open-ocean conditions~~due to the sea ice dynamics (McWilliams and Sullivan, 2000; Smyth et al., 2002; Brenner and Horvat, 2024).~~

. In the Arctic, sea ice modifies ~~upper ocean mixing dynamics in several ways. It limits~~ upper-ocean mixing by limiting wave fetch, ~~alters the directional spread~~ altering the directional distribution of wave energy, and ~~attenuates~~ preferentially attenuating short-wavelength ~~wave components- all of which reduce~~ components, thereby reducing both the magnitude and vertical extent of Stokes drift (Ardhuin et al., 2016, 2020; Li and Fox-Kemper, 2017). ~~Meanwhile~~At the same time, ice motion and floe interactions introduce additional sources of ~~surface~~ shear and turbulence (Skyllingstad and Denbo, 2001). ~~Observations show that waves propagate long distances under sea ice and significantly influence mixing near leads, polynyas, and the ice edge (Drucker et al., 2003; Kirillov et al., 2013; Horvat et al., 2020; Cooper et al., 2022). The presence of Langmuir cells in sea ice openings, confirms that the LT mechanism remains active in ice-covered waters, albeit with intermittent occurrence and modified structure (Dethleff and Kempema, 2007; Voermans et al., 2019). Although prior studies on wave - ice interactions have primarily focused on mechanical breakup of sea ice (Collins et al., 2018; Squire, 2018), the turbulent mixing contributions of LT in sea ice covered regions remain largely unexplored.~~ Recent modeling studies have ~~incorporated wave - ice interactions to investigate localized upper-ocean mixing (Horvat et al., 2016; Manucharyan and Thompson, 2017; Cooper et al., 2022; Brenner and Hor~~ ~~, but~~ begun to explore wave–ice interactions and localized mixing processes (Horvat et al., 2016; Manucharyan and Thompson, 2017; Coop . However, to our knowledge, no study has yet conducted a basin-wide, systematic evaluation of LT-drivenmixing potential under realistic Arctic sea ice and wave conditions.

In this study, we use a coupled sea ice - wave model that combines the neXtSIM Lagrangian sea ice model (Rampal et al., 2016) with the WAVEWATCH III (WW3) spectral wave model (Tolman et al., 2009). This modeling framework resolves surface Stokes drift, wave energy, and wind stress under evolving sea ice conditions. Using this information, we conduct an Arctic-wide assessment of LT mixing potential under realistic wave - sea ice interaction. *LT mixing potential* is defined as the amplitude of Langmuir forcing inferred from surface shear (friction velocity, u_*) and surface wave-induced Stokes drift at the surface ($u_{s(0)}$), independent of ~~oceanic dynamical adjustment~~the resulting oceanic response. Our primary objective is to identify when and where ~~LT mixing-supporting conditions~~ conditions favorable for LT mixing emerge and persist ~~, particularly in~~ in the Arctic in relation to seasonal sea ice advance and retreat. ~~To quantify the role of~~ We evaluate the applicability of open-ocean LT parameterizations in ice-covered regions, assessing their sensitivity to sea ice conditions. In particular, we examine how wind–wave ~~coupling, we compute both the standard (turbulent) Langmuir number La_t and the projected Langmuir number La_{proj}, incorporating the orientation angle α_{LOW} of Van Roekel et al. (2012), which represents the empirically derived rotation of Langmuir cells toward the combined Eulerian and Stokes contributions. Using these metrics, we map surface turbulent mixing regimes across space and time and estimate the seasonal evolution of TKE dissipation and vertical kinetic energy (VKE) associated with LT~~ misalignment, sea ice concentration, and seasonal evolution modulate LT forcing, and whether projected LT metrics are more sensitive to environmental forcing controlling mixing. Through this analysis, we aim to provide process-based constraints on LT parameterizations in the Arctic.

, where wave–ice interactions fundamentally alter the structure and efficiency of upper-ocean mixing. Section 2 details the coupled model configuration, the formulation of LT-relevant parameters, and ~~an evaluation of~~ the model inputs underpinning the LT metrics. Section 3 ~~beginning~~ begins with an assessment of LT-relevant wind and wave forcing in sea ice. We then ~~map~~ characterize the spatial and temporal organization of upper-ocean mixing ~~regimes and their variability~~ across the Arctic, ~~before examining~~ followed by an analysis of seasonal and regional patterns in ~~turbulent dissipation and normalized VKE~~mechanically forced dissipation and the the mixed-layer–averaged vertical velocity variance. Finally, we ~~assess~~ examine the influence of wind~~-~~–wave misalignment on LT energetics ~~, highlighting where projected Langmuir diagnostics diverge from canonical estimates~~and mixing. Section 4 discusses the implications of ~~our~~ these findings for Arctic mixed layer dynamics and model development, and outlines key limitations of the study.

2 Data and Methods

2.1 The neXtSIM- WAVEWATCH III coupled model

We use a coupled sea ice~~-~~–wave modeling framework that integrates the Lagrangian neXt-generation Sea Ice Model (neXtSIM) with the WAVEWATCH III (WW3) spectral wave model ~~using~~ through the OASIS-MCT coupler (Boutin et al., 2021). NeXtSIM provides ~~the~~ evolving sea ice concentration, thickness, and floe-size distribution (FSD)~~that~~ , which govern wave attenuation and the directional filtering of wave energy. Unlike Eulerian models, neXtSIM employs a moving triangular mesh ~~, undergoing~~ that undergoes periodic local remeshing to ~~retain~~ maintain a nominal resolution equivalent to the 25 km stereographic grid used by WW3. ~~Although the two components do not share the same mesh, fields are~~ The two components operate on different grids, with fields exchanged every 30 minutes via interpolation onto the WW3 exchange grid. NeXtSIM ~~receives atmospheric forcing from~~ is forced by the European Centre for Medium-Range Weather Forecasts (ECMWF) fifth generation reanalysis (ERA5) ~~and oceanic forcing from the Global Ocean Physics~~ atmospheric fields and the GLORYS12V1 ~~reanalysis, but it does not employ~~ ocean reanalysis, and does not impose lateral boundary conditions for sea ice. ~~Ice~~ Instead, sea ice drifts freely across ~~the~~ open boundaries, with ~~inflow treated as if external ice properties match those adjacent to the boundary (Ólason et al., 2025).~~

inflowing ice assumed to have properties consistent with the adjacent interior ice (Ólason et al., 2025). WW3 simulates wave propagation and attenuation in sea ice using the IS2+IC2 attenuation scheme, which ~~combines~~ accounts for scattering, inelastic flexure, and under-ice friction (Boutin et al., 2018). The southern boundary of the regional WW3 domain is ~~set~~ located at 54°N, ~~and~~ where lateral wave spectra are prescribed ~~along this open boundary~~ using the Ifremer global WW3 Modélisation et Analyse pour le Recherche Côtière (MARC) hindcast. WW3 is forced with the same ~~hourly~~ ERA5 winds ~~used to force neXtSIM, but as in standard WW3 configurations, no ocean currentsare applied~~as neXtSIM and does not include ocean currents, neglecting wave–current interactions. This configuration ~~has been shown to reproduce realistic wave-in-ice behaviour~~ reproduces realistic wave–ice interactions in the Barents and Beaufort Seas (Ardhuin et al., 2018) and yields MIZ extents consistent with ICESat-2 ~~altimeter~~ observations (Boutin et al., 2022).

~~Our simulations~~ Simulations cover the pan-Arctic domain for 2018–2022, with three-hourly output from the coupled ~~neXtSIM–WW3 model . This~~ system. At $25km$ grid resolution, the marginal ice is represented as a mesoscale transition zone, without resolving individual floes and small leads. Model configuration follows Boutin et al. (2022) and table S1 lists all model variables used in this study. The framework does not include a prognostic ocean mixed layer, so surface waves do not feed back on stratification or ~~vertical redistribution of turbulence. All~~ turbulence. Ocean stratification and MLD are prescribed from GLORYS12V1 reanalysis. Langmuir-related metrics presented here ~~therefore~~ represent the potential for mechanically forced ~~Langmuir turbulence implied by surface forcing , rather than~~ mixing inferred from surface forcing and do not capture the fully realized ~~upper-ocean response. The oceanic stratification and mixed layer depth (MLD) used in subsequent energetic diagnostics are prescribed independently from the GLORYS12V1 reanalysis, rather than evolving prognostically within the coupled system. This analysis thus quantifies the spatial structure of Langmuir-driven mixing implied by surface forcing alone. This definition is analogous to the Langmuir forcing framework of Li et al. (2019) and captures relative patterns of Langmuir activity even when absolute dissipation rates are not explicitly resolved.~~ ocean response.

The coupled ~~model~~ framework provides key advantages over ~~methods that only~~ approaches that combine sea ice fields with ~~ERA5 waves or rely on~~ externally derived wave products or empirical Stokes drift formulations (Webb and Fox-Kemper, 2011). In neXtSIM–WW3, Stokes drift and wave radiation stress are computed directly from the ice-attenuated wave spectrum, ~~rather than assuming open ocean conditions. Moreover, the prognostic FSD in neXtSIM~~ while the prognostic floe-size distribution modulates wave attenuation in a physically consistent manner~~, allowing the wave field to respond to floe fragmentation and the evolving seasonal morphology of the ice cover. By~~ . In contrast, ERA5 treats sea ice as land above a concentration threshold and ~~therefore cannot capture~~ cannot represent wave attenuation, directional filtering, or ~~the associated modulation of Stokes drift, processes that exert strong control on Langmuir forcing in the MIZ. Both models use the same physical parameters as the reference configuration described in Boutin et al. (2022). Table S1 in the Supplementary Material lists the wave, wind, sea ice , and surface ocean variables used in this study, either directly from model output or computed from established physical relationships~~their influence on Stokes drift. These processes are essential for capturing LT forcing in dynamic sea ice conditions, and for capturing how wave–ice interactions modify Lagrangian shear relevant to LT parameterizations.

2.2 Evaluation of model inputs relevant to LT metrics

To assess the fidelity of the neXtSIM–WW3 inputs most relevant for LT diagnostics, we evaluate the surface winds, surface shear, Stokes drift, and the representation of heterogeneous sea ice and MIZ conditions. ERA5 winds, which force both neXtSIM and WW3, ~~exhibit~~ show increased uncertainty under strong wind and high-latitude conditions, particularly near sharp ice–open-water transitions. Consistent with this, comparison against Cross-Calibrated Multi-Platform (CCMP) v3.1 data shows that ERA5 winds are systematically weaker than satellite-derived winds, and that this bias propagates directly into the diagnosed friction velocity u_*. Over 2018–2022, area-weighted Arctic mean 10-m winds ~~exhibit~~ shows a mean bias of -1.46 m s^{-1} (ERA5–CCMP), an RMSE of 1.47 m s^{-1}, and a correlation of 0.99 (Fig. S1), indicating high fidelity in synoptic variability despite a low mean state bias. Because CCMP assimilates ERA5 as a background field, this comparison primarily constrains mean state uncertainty.

The fidelity of neXtSIM sea ice concentration, ice-edge location, and deformation has been demonstrated in multiple studies. Ólason et al. (2025) report pan-Arctic sea ice extent RMSE of 0.76×10^6 km^2 and show that neXtSIM reproduces observed patterns of ice drift and deformation from OSI-SAF products, supporting its ability to represent heterogeneous ice fields that modulate wave penetration and Stokes drift pathways.

Accurate estimation of Stokes drift $u_{s(0)}$ further depends on realistic representation of short-wave attenuation in ice. The IS2+IC2 attenuation scheme implemented in WW3 has been shown to reproduce observed wave decay and spectral evolution in the Beaufort MIZ (Ardhuin et al., 2018), and to yield realistic pan-Arctic MIZ extents and wave-affected ice regimes consistent with ICESat-2–derived freeboard variability and floe-scale ice properties (Boutin et al., 2022). Based on sensitivity analyses and independent observational constraints, prior studies indicate that residual uncertainty in the short-wave spectrum, and hence in inferred Stokes drift, is dominated by uncertainties in wind forcing and sea ice concentration, with magnitude on the order of tens of percent rather than order-unity errors (Ardhuin et al., 2018; Boutin et al., 2022).

2.3 Surface stress partitioning and wind–wave forcing

To characterize momentum input into the ocean mixed layer under partial ice cover, we compute an effective surface stress that partitions momentum between the ice–ocean and atmosphere–ocean interfaces. Following the framework of Brenner et al. (2021), the net ocean surface stress is defined as an area-weighted combination of ice–ocean and atmosphere–ocean stresses, scaled by the local sea ice concentration:

$$\boldsymbol{\tau}_{ocn} = A\boldsymbol{\tau}_{io} + (1-A)\boldsymbol{\tau}_{ao} \tag{1}$$

where A is the sea ice concentration (0 = open ocean, 1 = fully ice covered), and the direct atmosphere–ocean stress is given by:

$$\boldsymbol{\tau}_{ao} = \rho_a C_{ao} |\mathbf{u}_a| \mathbf{u}_a \tag{2}$$

with with ρ_a as air density, $\mathbf{u}_a$ the 10-m wind velocity, and C_{ao} the air–sea drag coefficient over open water. Subsequently, we define an effective water-side friction velocity u_*, which represents the shear strength associated with the net surface stress transmitted to the ocean under partial ice cover:

$$u_* = \sqrt{\frac{|\boldsymbol{\tau}_{ocn}|}{\rho_o}}. \tag{3}$$

where ρ_o is the density of seawater. It provides the fundamental scaling for wind-driven mixing processes. The net surface stress $\boldsymbol{\tau}_{ao}$ represents an upper bound on the momentum flux available to drive mixed-layer shear during periods of active wave growth. This primarily affects the absolute magnitude of the diagnosed friction velocity u_*, while its spatial structure and relative variability remain more robust.

In addition to wind shear, surface waves ~~contribute~~ modify upper-ocean momentum through Stokes drift, the net Lagrangian transport of water particles ~~due to~~ arising from wave orbital motion. In WW3, the surface Stokes drift components (z = 0) are computed from the two-dimensional wave energy spectrum $F(k,\theta)$ as:

$$U_{sx}^{z=0} = g\int\int \frac{k^2\cos(\theta)}{\sigma^2}F(k,\theta)\,d\theta\,dk, \tag{4}$$

and

$$U_{sy}^{z=0} = g\int\int \frac{k^2\sin(\theta)}{\sigma^2}F(k,\theta)\,d\theta\,dk. \tag{5}$$

Here, σ is the wave frequency, k is the wave number and θ the propagation direction. These expressions define the eastward and northward components of the surface Stokes drift vector u_s. The effective friction velocity and surface Stokes drift ~~combined, provide two primary dynamical inputs required to evaluate *the potential for LT*~~ together characterize the surface shear and wave forcing that govern the mixing potential for LT under varying sea ice conditions.

2.4 Langmuir turbulence metrics in the Arctic

The Langmuir number (La_t) is a widely used parameter for quantifying the relative contributions of wind stress and wave-induced Stokes drift to upper ocean turbulence ~~(McWilliams and Sullivan, 2000)~~(McWilliams et al., 1997). It is defined as:

$$La_t = \sqrt{\frac{u_*}{u_{s(0)}}}, \tag{6}$$

where u_* is the friction velocity associated with the effective surface stress applied to the ocean, and $u_{s(0)}$ is the surface Stokes drift magnitude. In the open ocean, typical values of La_t range between 0.2 and 0.5 (Belcher et al., 2012), suggesting strong wave influence and active Langmuir circulation development, although La_t can reach values near or above 1 when wave effects are weak and wind-driven processes dominate (McWilliams et al., 1997; Belcher et al., 2012). These ranges are consistent with results from LES and field observations showing that stronger LT and deeper mixing are associated with lower La_t ~~(Harcourt, 2015)~~(Harcourt and D'Asaro, 2008). La_t is used in ocean modeling as a diagnostic of upper-ocean mixing regimes and to inform turbulence parameterizations. However, the traditional formulation implicitly assumes that the wind stress and Stokes drift are aligned. In realistic wave fields, especially in the Arctic, where mixed swell, turning winds, and ice-induced attenuation are common, misalignment can strongly reduce the effective Stokes shear that drives Langmuir circulations (Kukulka et al., 2010; Van Roekel et al., 2012; Li and Fox-Kemper, 2017).

To account for wind–wave misalignment, we adopt the *projected* Langmuir number of Van Roekel et al. (2012), which incorporates the dynamic orientation of the dominant Langmuir cells. In this framework, Langmuir cells do not necessarily align with the wind, but with the direction of maximum Lagrangian shear, set by a balance between Eulerian shear, Stokes drift, stratification, and Coriolis rotation. The ~~dynamic~~ orientation angle α_L represents the direction of the dominant Langmuir cells relative to the wind. Incorporating this angle yields the generalized projected Langmuir number:

$$La_{\text{proj}} \equiv \left(\frac{|u_*|\cos(\alpha_L)}{|u_{s(0)}|\cos(\theta_{ww}-\alpha_L)}\right)^{1/2}, \tag{7}$$

where θ_{ww} is the angle between the wind stress and Stokes drift vectors. ~~Equation (7) captures two effects: (i) the reduced wind-driven shear along the Langmuir cell axis via $\cos(\alpha_L)$, and (ii) the projected of Stokes forcing along that same axis via $\cos(\theta_{ww} - \alpha_L)$.~~

~~Direct evaluation of α_L requires resolving the~~ The Langmuir cell orientation $\alpha_{\rm L}$ depends on the vertical structure of ~~the Lagrangian shear , which is not feasible at the ∼ 25 km resolution of our pan-Arctic model. We therefore use the low-order wave (LOW)~~ Lagrangian shear and cannot be directly evaluated from surface forcing alone. We use the bulk approximation $\alpha_{\rm LOW}$ proposed by Van Roekel et al. (2012), which provides an ~~empirical estimate of Langmuir cell orientation by combining Eulerian shear and surface-layer Stokes shear~~ *a priori* estimate of the cell orientation based on depth-averaged Lagrangian shear. This estimate assumes that the Eulerian shear follows a law-of-the-wall profile, that cross-wind shear is negligible, and that Stokes shear is known from wave fields. The Lagrangian shear is expressed as the sum of Eulerian and Stokes contributions, with the Eulerian shear represented using a law-of-the-wall profile:

$$\tan\alpha_{\rm LOW} \approx \frac{\langle \partial v_s/\partial z\rangle_{D_L}}{\langle -u_*/(\kappa z) + \partial u_s/\partial z\rangle_{D_L}}, \tag{8}$$

where angle brackets denote a depth average over the Langmuir-affected layer D_L, and κ is the von Kármán constant. ~~LES results show that $\alpha_{\rm LOW}$ captures the orientation of Langmuir cells over a wide range of wind–wave misalignment angles, making it suitable for large-scale applications~~ This approximation provides a practical estimate of Langmuir cell orientation across a range of wind–wave misalignment conditions in LES, although it remains an idealized representation (Van Roekel et al., 2012).

~~In situations with strong wind–wave misalignment, $\alpha_{\rm LOW}$ typically reduces the effective projection of the Stokes drift into the Langmuir cell direction, partially counteracting the muted Langmuir response obtained when misalignment is represented solely by θ_{ww}. Hence, in our analysis, we we substitute $\alpha_{\rm LOW}$ for α_L in Eq. (7), yielding~~

$$La_{\rm proj} = \left(\frac{|u_*|\cos(\alpha_{\rm LOW})}{|u_{s(0)}|\cos(\theta_{ww} - \alpha_{\rm LOW})}\right)^{1/2}.$$

2.4.1 Surface forcing metrics and mixing regime classification

We introduce two complementary metrics to evaluate the ~~potential for LT~~ LT mixing potential under partial sea ice cover. The first evaluates how frequently surface forcing beneath sea ice resembles open-water conditions, based on exceedance metrics for surface stress and wave forcing. The second classifies near-surface ocean conditions into discrete mixing regimes based on the Langmuir number La_t and tracks transitions between these regimes over space and time.

We define exceedance metrics to quantify how often the near-surface wind and wave forcing in ice-covered regions approaches values typical of ~~open water~~the ones in open ocean. The two primary LT drivers considered are the surface friction velocity (u_*) and the surface Stokes drift velocity ($u_{s(0)}$). For each season (s) and grid cell (x,y), we define an open-water (OW) benchmark by computing the median value of a given variable X over all ice-free conditions (~~SIC < 0.15~~$SIC < 0.15$):

$$X_{\rm OW}^{(s)} = \mathrm{median}\{X_t(x,y)\,:\,\mathrm{SIC}_t(x,y) < 0.15,\ t \in s\}\,. \tag{9}$$

This benchmark represents the typical magnitude of atmosphere-~~-~~ocean or wave-induced surface forcing under ice-free conditions during a given season.

At each ice-covered grid cell (SIC ≥ 0.15), we compute the fraction of time steps for which the local value exceeds the seasonal OW benchmark. For a single variable, the exceedance metric is defined as

$$\text{Exceedance}_X^{(s)}(x,y) = \frac{N_t\left[\text{SIC}_t(x,y) \geq 0.15 \,\wedge\, X_t(x,y) \geq X_{\text{OW}}^{(s)}\right]}{N_t\left[\text{SIC}_t(x,y) \geq 0.15\right]}, \tag{10}$$

where $N_t[\cdot]$ denotes the number of seasonal time steps satisfying the specified condition. Seasons follow meteorological definitions: winter (DJF), spring (MAM), summer (JJA), and fall (SON). Grid cells are defined on a stereographic grid with approximately uniform spacing (25 km), such that their areas are effectively equal and statistics based on grid cell counts approximate area-weighted statistics.

To isolate conditions most relevant for ~~Langmuir turbulence~~LT, we further define a joint exceedance metric that quantifies the fraction of ice-covered time during which both surface friction velocity and surface Stokes drift simultaneously exceed their respective OW seasonal medians:

$$\text{JointExceedance}^{(s)}(x,y) = \frac{N_t\left[\text{SIC}_t(x,y) \geq 0.15 \,\wedge\, u_{*,t}(x,y) \geq u_{*,\text{OW}}^{(s)} \,\wedge\, u_{s(0),t}(x,y) \geq u_{s(0),\text{OW}}^{(s)}\right]}{N_t\left[\text{SIC}_t(x,y) \geq 0.15\right]}. \tag{11}$$

These exceedance metrics provide a physically interpretable measure of the frequency and persistence of LT-relevant surface forcing in ice-covered regions, relative to open-ocean benchmarks. As the OW benchmark varies seasonally, exceedance reflects relative forcing intensity and should be interpreted in the context of seasonal variability in OW conditions.

To characterize the evolving balance between wind-~~driven~~and wave-driven mixing, we classify surface forcing into three ~~distinct regimes based on~~ regimes using the turbulent Langmuir number La_t (Li et al., 2019). This classification represents a reduced, one-dimensional approximation of LES-based regime diagrams, which are formally defined in terms of both La_t and a stability parameter h/L_L, where h is the MLD and L_L is a Langmuir stability length scale that incorporates buoyancy forcing. Because our framework does not explicitly resolve buoyancy forcing or prognostic mixed layer dynamics, we collapse this two-parameter space onto La_t alone and adopt representative thresholds to distinguish wave-dominated, shear-dominated, and intermediate mixed-forcing conditions. At each time step T and grid cell (x,y), the regime is defined as:

$$\mathcal{R}(x,y,T) = \begin{cases} 1 & \text{if } La_t(x,y,T) > 0.94 \quad \text{(Shear-dominated)} \\ 2 & \text{if } 0.43 < La_t(x,y,T) \leq 0.94 \quad \text{(Mixed-forcing)} \\ 3 & \text{if } La_t(x,y,T) \leq 0.43 \quad \text{(Wave-dominated).} \end{cases} \tag{12}$$

To relate mixing regimes to sea ice conditions, we define spatial regions $\Omega(T)$ at each time step based on the local sea ice ~~concentration SIC(x,y,T):~~

$$\Omega_{\text{ice}}(T) = \{(x,y)\,|\,\text{SIC}(x,y,T) > 0.8\},$$

$$\Omega_{\text{MIZ}}(T) = \{(x,y)\,|\,0.15 \leq \text{SIC}(x,y,T) \leq 0.8\},$$

$$\Omega_{\text{OW}}(T) = \{(x,y)\,|\,\text{SIC}(x,y,T) < 0.15\}.$$

$$\begin{aligned}\Omega_{\text{ice}}(T) &= \{(x,y)\mid \text{SIC}(x,y,T) > 0.8\},\\ \Omega_{\text{MIZ}}(T) &= \{(x,y)\mid 0.15 \leq \text{SIC}(x,y,T) \leq 0.8\},\\ \Omega_{\text{OW}}(T) &= \{(x,y)\mid \text{SIC}(x,y,T) < 0.15\}.\end{aligned} \tag{13}$$

For each region Ω and regime $r \in \{1,2,3\}$, we compute the spatial fraction of grid cells occupying regime r at time T as

$$f_r^{\Omega}(T) = \frac{1}{|\Omega(T)|} \sum_{(x,y)\in\Omega(T)} \delta(\mathcal{R}(x,y,T) = r)\,, \tag{14}$$

where $\delta(\cdot)$ is the indicator function and $|\Omega(T)|$ is the number of valid grid cells in region $\Omega(T)$.

Beyond regime occupancy, we assess the temporal stability of the surface forcing balance by tracking transitions between regimes. For each grid cell (x,y), we count transitions from regime r_n to r_m between successive time steps, restricted to periods when the grid cell remains within the same ice regime Ω:

$$T^{\Omega}_{r_n\to r_m}(x,y) = \sum_{T=2}^{T_{\max}} \delta(\mathcal{R}(x,y,T-1) = r_n)\,\delta(\mathcal{R}(x,y,T) = r_m)\,\delta((x,y)\in\Omega(T-1)\cap\Omega(T))\,. \tag{15}$$

Spatial differences in temporal sampling are evaluated using transition counts, normalized by the number of time steps a grid cell resides within region Ω,

$$\bar{T}^{\Omega}_{r_n\to r_m}(x,y) = \frac{T^{\Omega}_{r_n\to r_m}(x,y)}{N_{\Omega}(x,y)}, \tag{16}$$

where $N_{\Omega}(x,y)$ denotes the total number of time steps satisfying the regional criterion. The resulting normalized transition frequency provides a measure of how often the dominant surface forcing balance reorganizes at a given location over the analysis period.

2.4.2 Langmuir Turbulence Energetics

To examine how LT modifies upper-ocean energetics, we evaluate two complementary metrics ~~derived from~~ based on the vertically integrated turbulent kinetic energy (TKE) budget: (i) the mixed-layer–averaged vertical velocity variance, $\langle w'^2\rangle_{H_{ML}}$, and (ii) the ~~TKE~~ mechanically driven dissipation rate, ~~ε~~ $\varepsilon_{\text{mech}}$. Both are ~~based on empirically derived LES scalings, but they~~

~~characterize distinct aspects of the turbulent response~~derived from empirically based LES scalings and provide complementary diagnostics of turbulence intensity and energy dissipation.

We compute $\langle w'^2\rangle_{H_{ML}}$ following the LES-based scaling of Van Roekel et al. (2012):

$$\langle w'^2\rangle_{H_{ML}} = 0.6\,[u_*\cos(\alpha_{\mathrm{LOW}})]^2\left(1+(c_1 La_x)^{-2}+(c_2 La_x)^{-4}\right), \tag{17}$$

where u_* is the friction velocity and La_x denotes the Langmuir number metric used in the scaling. The La_x^{-2} and La_x^{-4} terms capture the nonlinear enhancement of vertical velocity variance by Langmuir forcing, with lower Langmuir numbers indicating stronger turbulence. The projection factor $\cos(\alpha_{\mathrm{LOW}})$ ~~ensures that vertical velocity is appropriately scaled along the Langmuir cell axis~~accounts for the orientation of Langmuir cells relative to the wind. For the ~~turbulent Langmuir number~~wind-aligned case, we set $La_x = La_t$ and $\alpha_{\mathrm{LOW}} = 0$, ~~corresponding to Langmuir cells aligned with the wind~~, while for the projected formulation we use $La_x = La_{\mathrm{proj}}$. We adopt $(c_1, c_2) = (3.1, 5.7)$ for La_t and $(c_1, c_2) = (3.1, 5.4)$ for La_{proj}, consistent with the original LES fits following Van Roekel et al. (2012). ~~The scaling in Eq. (17) was derived under conditions of~~ Because this scaling is derived under weak or destabilizing ~~surface buoyancy flux in LES. Because Arctic mixed layers are frequently stabilized by ice melt and freshwater input, the diagnosed~~ buoyancy forcing, the resulting values of $\langle w'^2\rangle_{H_{ML}}$ ~~should be~~ are interpreted as a measure of LT ~~potential, rather than as~~ mixing potential rather than a direct prediction of the realized turbulent state.

The contribution of LT to upper-ocean energy dissipation is ~~quantified using a vertically integrated turbulent kinetic energy (TKE) scaling framework following~~ estimated using a reduced form of the scaling framework of Belcher et al. (2012). In the mixed-layer interior, ~~away from the near-surface wave-breaking region, the turbulent dissipation rate~~ turbulent dissipation can be approximated as the sum of contributions from ~~wind-driven~~ shear, Stokes drift~~(Langmuir turbulence), and surface~~ , and buoyancy forcing. Factoring out the shear-based velocity scale yields:

$$\varepsilon \sim \frac{u_*^3}{H_{\mathrm{ML}}}\left[A_s + A_L\,La_x^{-2} + A_c\,\frac{B_s H_{\mathrm{ML}}}{u_*^3}\right], \tag{18}$$

where H_{ML} is the mixed-layer depth, La_x ~~is a Langmuir number metric characterizing~~ characterizes the relative importance of wave forcing~~to shear~~, and B_s is the surface buoyancy flux. The ~~constants~~ coefficients A_s, A_L, and A_c are empirical ~~coefficients~~ constants of order unity ~~that represent the efficiency of~~ representing shear-, Langmuir-, and buoyancy-driven ~~turbulence~~contributions, respectively.

The Langmuir contribution ~~in Eq. (18)~~ scales as La_x^{-2}, ~~reflecting~~ consistent with the ratio of ~~the Stokes drift velocity scale to the friction velocity , u_s/u_*. This scaling is consistent with the Langmuir velocity scale $w_{*L} = (u_*^2 u_s)^{1/3}$~~ Stokes drift to friction velocity and with LES results ~~demonstrating enhanced interior~~ showing enhanced mixing under strong ~~wind–wave coupling(Belcher et al., 2012; Van Roekel et al., 2012)~~wind–wave coupling.

Consistent with the ~~surface forcing-only~~ surface-forcing-only framework described in Section 2.1, we omit the buoyancy-~~dependent~~contr in Eq. ~~(18)~~ (19) and adopt a reduced formulation that isolates mechanically driven turbulence~~. We define a mechanically forced~~

~~dissipation scale as:~~ :

$$\varepsilon_{\mathrm{mech}} = \frac{u_*^3}{H_{\mathrm{ML}}}\left(1+\beta\,La_x^{-2}\right), \tag{19}$$

where the second term represents enhancement of ~~turbulent~~ dissipation by wave-induced Stokes drift. The empirical coefficient β parameterizes the efficiency ~~with which LT augments mechanically driven dissipation~~ of this enhancement, with LES suggesting $\beta \approx 0.15$ under weakly stratified conditions. ~~LES in open-ocean settings suggest $\beta \approx 0.15$. We emphasize that~~ The resulting $\varepsilon_{\mathrm{mech}}$ is ~~an energetic proxy rather than a full representation of turbulent dissipation, as it neglects buoyancy production, entrainment, and stratification-dependent suppression. Its purpose here is to quantify the spatial and temporal variability of~~ used here as a diagnostic of mechanically mediated energy input associated with wind~~and wave forcing , providing a physically interpretable metric for comparing mixing regimes within the MIZ~~–wave forcing and is interpreted as a proxy for LT-driven mixing potential.

~~We adopt a reanalysis-derived~~ The mixed-layer depth H_{ML} ~~as a physically consistent bulk depth scale rather than a real-time boundary-layer estimate. Specifically, we use~~ is taken from the GLORYS12 reanalysis~~(0.08° resolution), computed daily and remapped to the 25 km model grid~~, which provides a spatially and seasonally varying vertical scale for interpreting mechanically forced turbulence. Although GLORYS12 does not explicitly resolve ice-modified boundary-layer processes, ~~its~~ it offers a physically consistent bulk estimate of the mixed-layer ~~depth provides a physically grounded, spatially and seasonally varying vertical scale over which mechanically forced turbulence can be interpreted in a vertically integrated sense. Equation (**??**) is therefore interpreted as an effective dissipation scaling rather than a closed TKE budget, and is used here as a diagnostic of LT potential under wind–wave forcing~~depth suitable for vertically integrated diagnostics.

All spatial statistics are computed on the model exchange grid, which has an approximately uniform 25 km resolution in the polar stereographic projection. Grid cell area varies slightly with latitude, but cosine-latitude weighting yields negligible differences, indicating that grid-cell-based statistics are representative of area-weighted behavior.

3 Results

3.1 Spatiotemporal variability of surface forcing across the Arctic

~~Figure 1 presents the seasonal distribution of joint exceedance of open-water (OW) -like surface forcingover the five-year simulation period. Across~~

Figure 1 summarizes the seasonal variability of surface forcing through open-water (OW) exceedance of friction velocity (u_*), Stokes drift ($u_{s(0)}$), and their joint occurrence (see Eqs. 10–11). The top panels show probability density functions (PDFs) of exceedance fractions across all ice-covered grid cells ($SIC \geq 0.15$), and the bottom panels map the spatial distribution of joint exceedance relative to seasonal median sea ice concentration (SIC) contours. The PDFs (Fig. 1a–c) reveal an asymmetry between atmospheric and wave forcing. Exceedance of wind stress (u_*) spans a broad range across all seasons, ~~joint exceedance is generally low~~ indicating that atmospheric forcing in ice-covered regions frequently reaches magnitudes comparable to OW conditions. In contrast, Stokes drift ($u_{s(0)}$) exceedance is strongly skewed toward low values, with a rapid decay toward higher exceedance fractions, reflecting the attenuation of wave energy within ice-covered regions (Liu and Mollo-Christensen, 1988; Ardhuin et al . As a result, joint exceedance closely follows the Stokes drift distribution, highlighting the dominant role of wave forcing in setting LT-relevant mixing conditions.

Spatially (Fig. 1d–g), ~~with values rarely exceeding 0.2, indicating that conditions comparable to OW, where strong winds and waves act simultaneously, occur only infrequently in sea ice. Where it does occur,~~ joint exceedance is ~~spatially confined and predominantly~~ concentrated along the ~~seasonal sea ice edge~~MIZ, closely aligned with the 15–80% SIC contours. The highest ~~values are consistently~~ occurrence is found in the Barents, Greenland, and Chukchi Seas, ~~regions where ice cover is thinner, more mobile, and more frequently disrupted.~~

~~The spatial distribution exhibits clear seasonal contrasts~~where fragmented, mobile ice reduces wave attenuation and allows intermittent penetration of wave energy into the ice-covered ocean. Because the OW benchmark is defined separately for each season, exceedance represents a measure of relative forcing intensity rather than absolute magnitude. Across all seasons, joint exceedance remains limited, rarely exceeding 0.2, indicating that simultaneous strong wind and wave forcing beneath sea ice is uncommon. Seasonal differences therefore reflect both variations in forcing and shifts in the reference state. During winter and ~~the~~ transitional seasons (DJF, MAM, SON), ~~joint exceedance is stronger and~~ exceedance is more spatially continuous along the MIZ, ~~reflecting the increased likelihood of~~ consistent with enhanced wave–ice interaction under storm-driven ~~conditions interacting with loosely consolidated ice .~~ conditions. However, winter shows comparatively low exceedance despite strong winds and wave heights, because the open-water reference state is also elevated, raising the threshold for exceedance. In contrast, ~~summer (JJA~~fall (SON) shows the ~~weakest joint exceedance overall. However, exceedance events in summer are more geographically dispersed, suggesting that while LT-relevant forcing is rarer, it can still intermittently extend into areas classified as pack ice.This scattered summer signal highlights the potential for episodic Langmuir turbulence beyond the immediate MIZ during the melt season.~~ ~~**Seasonal joint exceedance of wind–wave surface forcing beneath Arctic sea ice.**~~ ~~Panels (a–d) show, for each season, the fraction of under-ice time ($SIC \geq 0.15$) during which both surface friction velocity u_* and surface Stokes drift $u_{s(0)}$ simultaneously exceed their respective seasonal open-water medians ($SIC < 0.15$). Elevated values (yellow–orange) indicate locations where wind-driven shear and residual wave-driven drift intermittently reach open-water–like magnitudes despite the presence of sea ice. A nonlinear (power-law) color scaling is applied to enhance contrast at low exceedance fractions, emphasizing spatial variability in rare joint exceedance events. Dashed and solid contours denote the seasonal mean~~ ~~**15%**~~ ~~(teal) and~~ ~~**80%**~~ ~~(blue) sea ice concentration boundaries, respectively, providing context for the typical extent of the marginal ice zone and the transition to the consolidated pack. Joint exceedance is shown only at grid cells that experience sea ice conditions at least once during each season.~~

~~To provide additional physical context for this seasonal asymmetry, Supplementary Figure~~highest frequency of elevated joint exceedance values, even though wave heights are more moderate than in winter (Fig. S2~~summarizes the distribution of significant wave height (H_s)within the marginal ice zone (MIZ) across seasons. Winter (DJF) exhibits both the highest median wave heights and the largest spread, consistent with frequent storm-driven wave events capable of penetrating into partially ice-covered regions. In contrast, summer~~). This reflects the combination of a lower open-water reference and more efficient wave penetration into fragmented ice cover, allowing sea ice conditions to more frequently approach OW forcing. Summer

(JJA) ~~wave heights are strongly suppressed, with low median values and limited variability, consistent with reduced Stokes drift forcing even where ice cover is fragmented. The transitional seasons (MAM, SON) exhibit intermediate behavior, characterized by lower median wave heights but pronounced upper tails, reflecting episodic wave events rather than sustained wave forcing.~~ shows a different regime. Weaker open-water winds and waves reduce the seasonal benchmark, such that moderate forcing more readily exceeds the reference. As a result, exceedance is spatially widespread. However, the magnitude of exceedance remains low, indicating that this broad signal corresponds to weak LT-relevant forcing.

~~Consistent with seasonal wave climate, the confinement of joint exceedance to the MIZ across all seasons highlights the role of sea ice state in regulating surface forcing. Reduced joint exceedance during summer reflects both diminished storm activity and enhanced attenuation of wave-induced Stokes drift within even moderately concentrated ice, in agreement with theoretical and observational studies documenting rapid decay of Stokes transport under partial ice cover (Ardhuin et al., 2016; Herman, 2017; Liu and . In contrast, the persistence of joint exceedance during winter and transitional seasons indicates that~~ Based on the exceedance metrics, LT-relevant mixing is primarily controlled by the availability and intermittency of wave forcing. Limited wave penetration beneath sea ice suppresses Stokes drift and inhibits LT, favoring predominantly shear-driven mixing, while episodic storm-driven events ~~can temporarily restore OW-like~~ in the MIZ can temporarily establish open-water-like forcing beneath the ice~~, even when mean conditions remain ice covered~~.

3.2 Mapping upper-ocean mixing regime dynamics in the Arctic

To further explore the controls on LT mixing potential, we examine the spatial and seasonal structure of the turbulent Langmuir number (La_t). All La_t medians are computed over the full spatial domain shown in Figure 2, without restricting the analysis based on sea ice concentration. The five-year climatological median (Figure 2a) reveals a persistent band of low La_t encircling the perennial ice pack and closely following the climatological 15% SIC contour and consistent with patterns shown in Figure 1. Elevated median La_t values (> 1) dominate the central Arctic under compact ice cover, indicating ~~regimes where wave influenceis weak and surface shear governs upper-ocean mixing~~a shear-dominated mixing regime with limited wave influence. In contrast, moderate to low median La_t values (< 0.45), which ~~indicate some LT~~ show LT mixing potential, are confined to narrow, seasonally evolving bands along the ice edge. ~~Under open-ocean~~ In OW conditions (SIC < 0.15), median La_t values are generally below 0.35, consistent with the range identified by Belcher et al. (2012) as favorable for LT ~~conditions. This large-scale spatial structure reflects the progressive suppression of wave-induced Stokes transport with increasing ice concentration, as LT potential diminishes when Stokes production weakens relative to shear production.~~ mixing. The spatial and seasonal patterns in La_t closely reflect the exceedance statistics, reinforcing that wave-driven mixing is intermittent and strongly modulated by the sea ice cover. As ice concentration increases, wave attenuation limits Stokes-driven forcing, shifting the balance toward shear-dominated mixing and reducing LT mixing potential.

Seasonal medians (Figures 2b–e) further ~~illustrate~~ depict how transitions in ice state modulate the balance between wave and wind forcing. During winter and spring (Figures 2b–c), sharp gradients in La_t delineate the transition from wave-influenced conditions near the ice edge to shear-dominated regimes within the consolidated ice. ~~This abrupt shift reflects compact ice~~

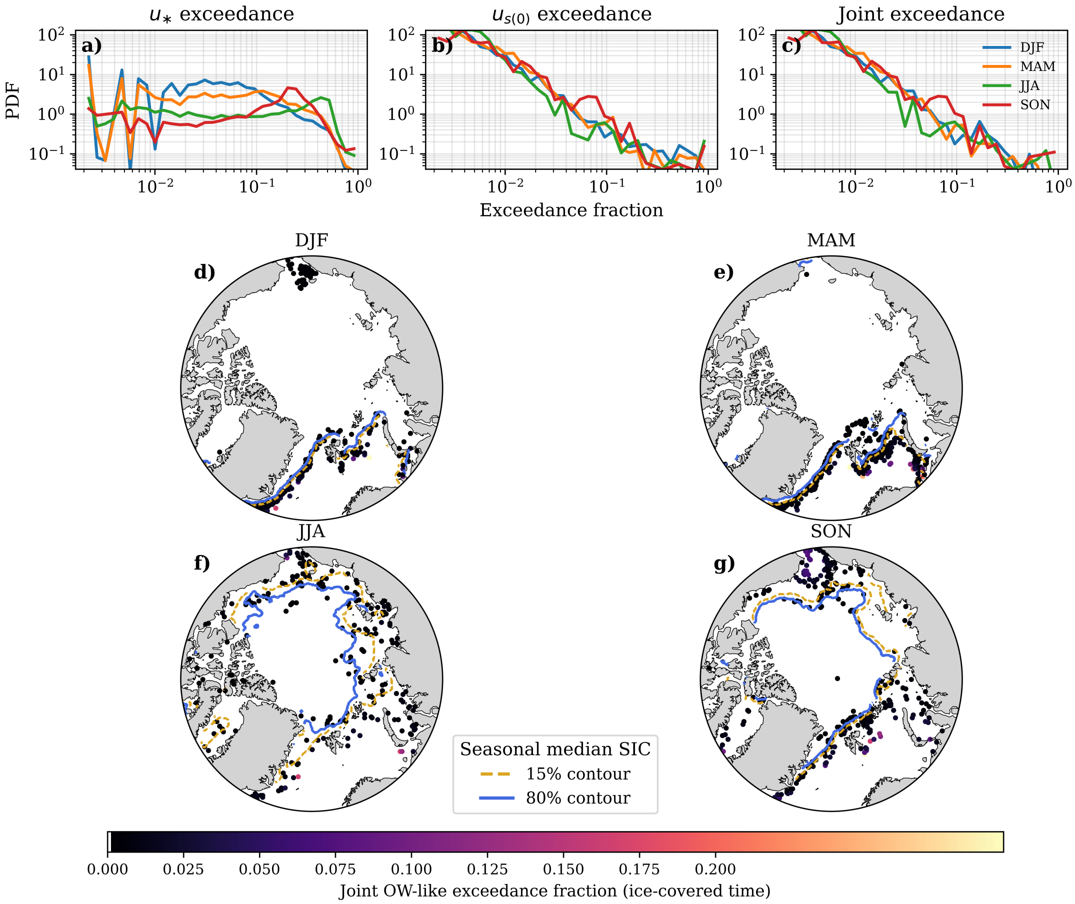

Figure 1. **Seasonal exceedance of wind–wave surface forcing beneath Arctic sea ice.** (a–c) Probability density functions (PDFs) of exceedance fractions for surface friction velocity (u_*), surface Stokes drift ($u_{s(0)}$), and their joint occurrence, computed over ice-covered conditions ($SIC \geq 0.15$) relative to seasonal open-water medians ($SIC < 0.15$). (d–g) Spatial distribution of the joint exceedance fraction, defined as the fraction of under-ice time during which both u_* and $u_{s(0)}$ simultaneously exceed their respective seasonal open-water medians. Elevated values (yellow–orange) indicate regions where wind and wave forcing intermittently reach open-ocean–like magnitudes despite the presence of sea ice. Dashed and solid contours denote the seasonal median **15%** (gold) and **80%** (blue) sea ice concentration boundaries, respectively, providing context for the marginal ice zone and consolidated pack ice. Joint exceedance is shown only at grid cells that experience sea ice conditions at least once during each season.

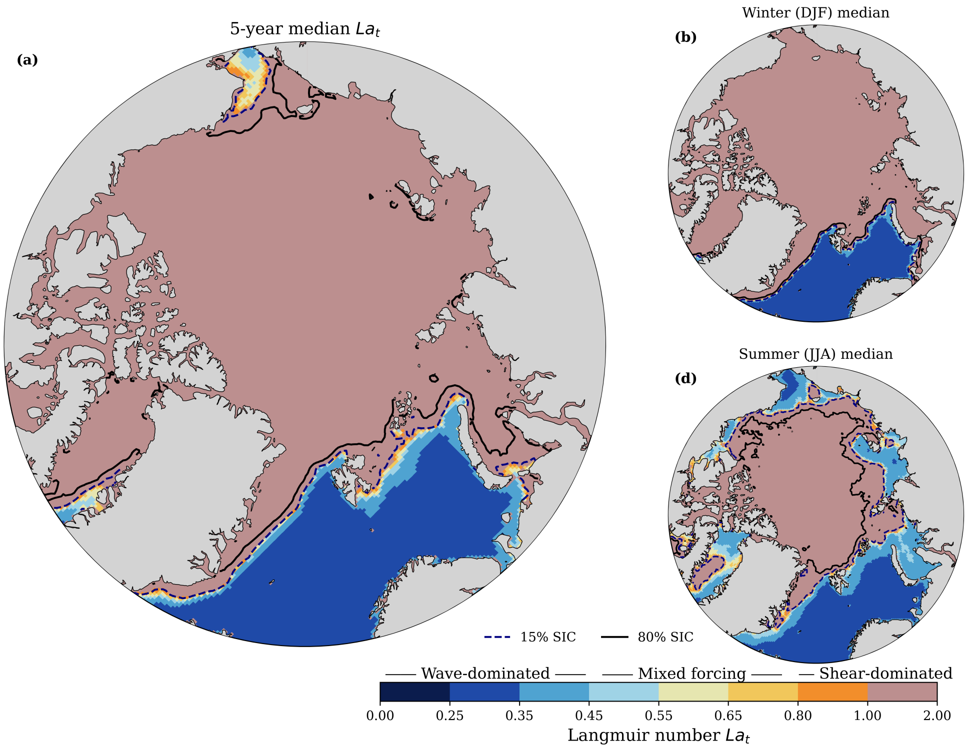

Figure 2. Spatial distribution of the median Langmuir number La_t, integrated over 2018 to 2022, along with its seasonal medians. Panel (a) shows the five-year climatological median of the Langmuir number La_t computed across all seasons. The median 15% and 80% SIC contours are overlaid in dashed dark blue and solid black ~~colors~~ lines marking the median SIC-defined extent of the MIZ across seasons. Panels (b–e) show the medians for winter (DJF), spring (MAM), summer (JJA), and fall (SON), respectively. In all panels, La_t is shown for all ocean grid cells without applying a SIC mask; SIC contours are overlaid for context.

~~cover and strong wave attenuation, which limit Stokes drift penetration beneath the ice even during~~ Compact ice cover strongly attenuates wave energy, limiting the penetration of Stokes drift in ice-covered regions, even under periods of strong wind forcing. In contrast, summer and fall (Figures 2d–e) ~~exhibit~~ show a broader and more continuous band of reduced La_t extending into the seasonal sea ice zone. ~~Increased OW exposure, enhanced fetch, and elevated wave activity during these seasons allow Stokes drift to penetrate farther beneath the ice, reducing La_t and promoting conditionsmore conducive to LT. These seasonal patterns indicate~~ Lower ice concentration and increased ice mobility can reduce wave attenuation and allow wave-driven forcing to extend farther into the seasonal MIZ, even without stronger wave conditions. These patterns reinforce that departures from open-ocean La_t values are primarily associated with modulation of Stokes drift by sea ice ~~rather than~~ combined with changes in wind forcing~~alone~~. The seasonal MIZ ~~therefore~~ emerges as a ~~dynamically~~ distinct transition zone~~in which~~, where the balance between shear- and wave-driven turbulence ~~shifts toward LT-favorable~~ can shift toward Langmuir-favorable conditions, while the interior pack ~~ice remains characterized by~~ remains persistently shear-dominated ~~mixing throughout the year~~year-round.

3.3 Mapping upper-ocean mixing regime dynamics in the Arctic

~~Figure~~

Figure 3 synthesizes the spatial structure, temporal variability, and persistence of upper-ocean mixing regimes under ~~consistent sea ice concentration ($SIC > 15\%$)conditions.~~ice-covered conditions ($SIC \geq 0.15$), based on the regime classification defined in Eq. (12) and the transition framework described in Eqs. (13–16). Panel (a) shows the dominant mixing regime at each grid cell, defined ~~by $\geq$~~as the regime occurring for at least 50% ~~seasonal persistence and quantified using Eq. (13).~~ of ice-covered time. The Arctic interior is characterized primarily by shear-driven mixing ($La_t \geq 0.94$), while mixed ($0.43 \leq La_t < 0.94$) and wave-driven ($La_t < 0.43$) regimes are confined to the seasonal MIZ and regions ~~proximal to~~ near the ice edge, where ~~surface-wave and wind~~ wind and wave forcing increasingly compete. Panel (~~b~~c) maps the normalized frequency of regime transitions~~at each grid cell~~, expressed as the number of regime changes per ice-covered day. Enhanced regime instability is strongly localized ~~to~~ within the MIZ, particularly along sectors exposed to episodic wave activity and intermittent ~~open-water conditions.~~ OW conditions. This spatial pattern is consistent with fetch-limited wave growth in partial ice cover, where intermittent Stokes drift enhances variability in the relative balance between wind and wave forcing (Brenner and Horvat, 2024) . In contrast, ~~the consolidated interior pack ice exhibits~~ pack ice has uniformly low transition rates, ~~indicative of~~ indicating stable and persistent forcing ~~balances throughout the year.~~ ~~**Spatial and temporal characteristics of upper-ocean mixing regime dynamics under sea ice for SIC $\geq$ 0.15.**~~ ~~(a) Dominant mixing regime defined as the regime occupying at least 50% of SIC-covered days at each grid cell over the analysis period. Shear-driven conditions dominate the compact ice interior, while mixed and wave-driven regimes preferentially occur near the ice edge and in seasonally ice-covered regions. Dashed and solid contours indicate the 15% and 80% sea ice concentration (SIC) thresholds, respectively. (b) Normalized regime transition frequency (transitions per SIC-covered day) for SIC $\geq$ 0.15, highlighting enhanced temporal variability along the MIZ and reduced variability within the compact ice interior. (c) Time series of marginal ice zone (MIZ; 0.15 $\leq$ SIC $\leq$ 0.8) regime instability, defined as the fraction of MIZ grid cells undergoing at least one regime transition within a 30-day window (black), together with the contemporaneous fraction of the Arctic domain classified as MIZ (blue, dashed). (d) Relationship between regime persistence and instability within the MIZ, shown as the median longest continuous regime duration (black) and interquartile range (shading) binned by the mean number of days between regime transitions. Increasing transition frequency is associated with a systematic reduction in regime persistence.~~ ~~The temporal evolution of regime instability within the MIZ is shown in panel (c), quantified~~ conditions. Localized transitions within consolidated ice likely reflect episodic openings (e.g., leads and polynyas) that temporarily allow wave generation and induce short-lived shifts in mixing regime.

Panels (b) and (d), restricted to MIZ grid cells ($0.15 \leq SIC \leq 0.8$), further resolve the temporal characteristics of regime variability. Regime instability (panel b), defined as the fraction of MIZ grid cells ~~(0.15 $\leq$ SIC $\leq$ 0.8) that undergo~~ undergoing at least one ~~regime~~ transition within a 30-day window~~. Regime instability exhibits pronounced seasonal modulation, with recurrent~~ , reveals a pronounced seasonal cycle with peaks during periods of ice advance and retreat. ~~Peaks in regime instability systematically~~ These peaks precede maxima in MIZ area, indicating ~~a temporal lag between dynamic reorganization and the geometric expansion ofthe SIC-defined MIZ~~ that enhanced regime variability occurs prior to, rather than as a consequence of, MIZ expansion. This behavior is consistent with wind, wave, and ice forcing becoming comparable during seasonal transitions in the MIZ, such that no single regime dominates. Small variations in forcing can shift the balance between regimes, leading to frequent transitions and elevated instability along the evolving MIZ boundary. ~~Periods of elevated instability correspond to times when grid cells reside near regime boundaries and experience strong competition between wind-, wave-, and ice-mediated forcing , whereas subsequent MIZexpansion reflects the integrated outcome of this reorganization.~~ Panel (d) ~~directly links~~ relates regime instability to persistence by ~~relating~~ comparing the mean time between regime transitions ~~to~~ with the longest continuous duration of a single regime within MIZ grid cells. Median regime persistence increases ~~monotonically with increasing time between transitions, however~~ with increasing inter-transition time, although the relationship is ~~highly non-linear, with persistence collapsing rapidly once transitions become more frequent. In our analysis, this collapse occurs~~ nonlinear. Persistence rises rapidly at short timescales before approaching a plateau at longer intervals, with the transition occurring at inter-transition timescales of ~~order several weeks , although the precise threshold varies spatially across the~~ approximately several weeks ($\sim$20–50 days), depending on location within the MIZ. The broad interquartile range at short transition ~~timescales~~ intervals reflects substantial variability ~~associated with intermittently forced regimes~~ in intermittently forced regions near the ice edge, ~~whereas longer transition times are associated with sustained ,~~ where regimes are frequently disrupted. In contrast, longer transition intervals correspond to more sustained and dynamically stable regimes. ~~Together, panels (c) and (d) indicate that mixing regime instability in the MIZ is governed by transient, event-driven forcing and precedes changes in MIZ extent. This phase offset indicates that regime instability is driven by the rate of ice and surface forcing evolution rather than by MIZ extent itself, with dynamically active transition periods dominating mixing regime variability~~Peak instability ($\sim$0.1 transitions per day) corresponds to approximately 2–3 transitions per month, with mean intervals of $\sim$10–30 days between transitions. Despite this relatively frequent switching, individual regimes persist for $\sim$50–150 days, increasing to $\sim$100–200 days under low transition frequencies. Overall, this indicates that MIZ uper ocean mixing is characterized by intermittent regime shifts superimposed on otherwise persistent states, rather than continuous or rapid switching, with regime evolution occurring on sub-seasonal timescales.

Figure 4 provides complementary ~~information~~ insight into how both local and spatially aggregated values of La_t ~~, depend on sea ice concentration (SIC)~~depend on SIC, and helps contextualize the spatial regime structure ~~identified~~ from in Figure 3. Panel (a) shows that median La_t generally increases with SIC across ~~most~~ all seasons, indicating a systematic shift toward shear-dominated ~~conditions~~ mixing as ice cover increases. Conditions associated with strong LT mixing potential ($La_t < 0.43$) are largely confined to OW or low SIC, whereas shear-dominated regimes ($La_t > 0.94$) ~~prevail~~ dominate at moderate to high SIC. This behavior is consistent with ~~the~~ increasing attenuation of wave energy and ~~reduction of~~ reduced Stokes drift under ~~partial ice cover~~higher ice concentrations. During summer, however, the relationship deviates from this monotonic trend. At high SIC ($\gtrsim 0.8$), median La_t ~~exhibits a reduction at high SIC. This deviation~~ decreases, indicating a relative increase in wave influence despite high ice concentration. Additional diagnostics (Fig. S3) show that in this regime La_t exhibits limited dependence on sea ice thickness, but decreases rapidly with increasing significant wave height (h_s) over the range 0–1 m. This suggests enhanced sensitivity of La_t to wave forcing, where even modest increases in wave height can substantially increase Stokes drift and reduce La_t. This is consistent with ~~seasonal changes in ice mechanical properties and surface forcing, under~~

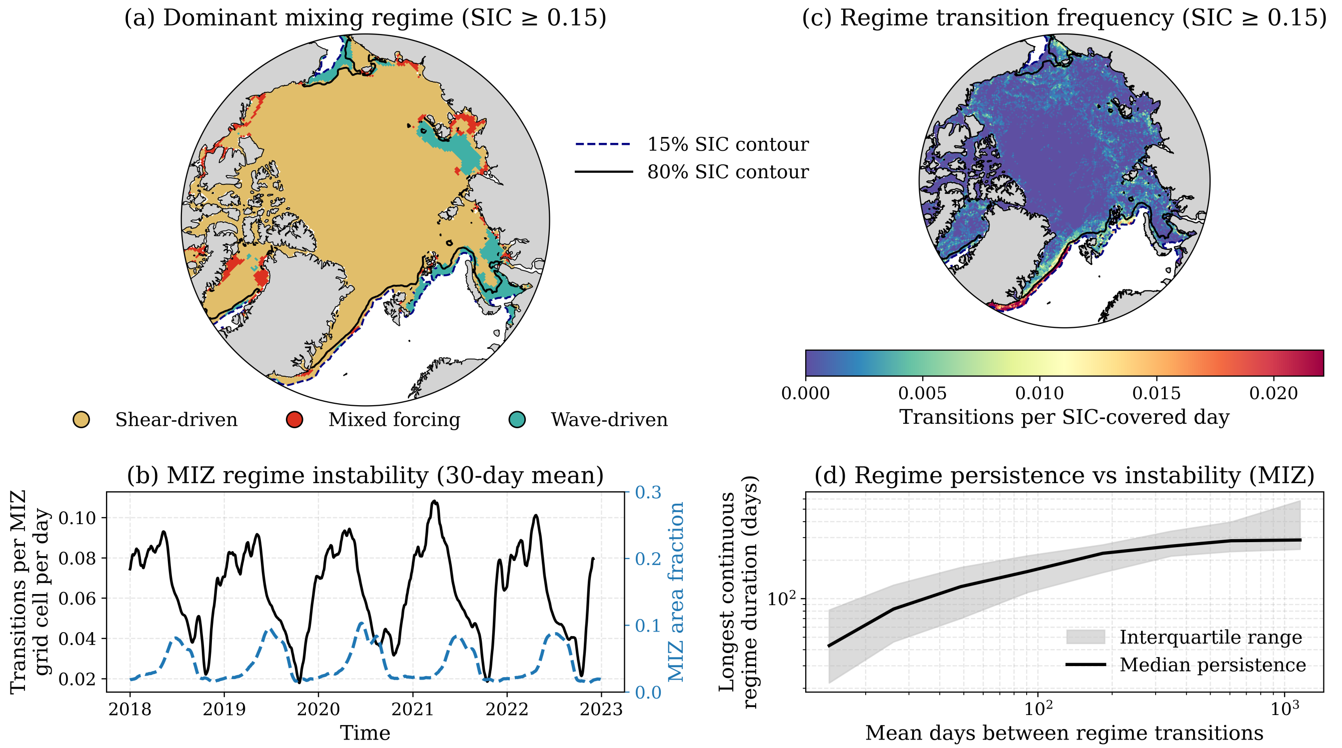

Figure 3. **Spatial and temporal characteristics of upper-ocean mixing regime dynamics under sea ice for SIC ≥ 0.15.** (a) Dominant mixing regime defined as the regime occupying at least 50% of SIC-covered days at each grid cell over the analysis period. Shear-driven conditions dominate the compact ice interior, while mixed and wave-driven regimes preferentially occur near the ice edge and in seasonally ice-covered regions. Dashed and solid contours indicate the 15% and 80% sea ice concentration (SIC) thresholds, respectively. (b) Time series of marginal ice zone (MIZ; $0.15 \leq \mathrm{SIC} \leq 0.8$) regime instability, defined as the fraction of MIZ grid cells undergoing at least one regime transition within a 30-day window (black), together with the contemporaneous fraction of the Arctic domain classified as MIZ (blue, dashed). (c) Normalized regime transition frequency (transitions per SIC-covered day) for SIC ≥ 0.15, highlighting enhanced temporal variability along the MIZ and reduced variability within the compact ice interior. (d) Relationship between regime persistence and instability within the MIZ, shown as the median longest continuous regime duration (black) and interquartile range (shading) binned by the mean number of days between regime transitions. Increasing transition frequency is associated with a systematic reduction in regime persistence.

~~which thinner and more fragmented ice with enhanced~~ melt-season conditions in which the ice cover becomes mechanically weakened and increasingly spatially heterogeneous. Partial fragmentation and floe-scale ~~heterogeneity may permit intermittent penetration of long-period swell into regions that remain nominally ice covered (Ardhuin et al., 2016; Brenner and Horvat, 2024). At the same time,~~ openings allow intermittent wave transmission or local, fetch-limited wave generation, while spatial variability in wind stress over melting ice ~~tends to be reduced and spatially variable, which can diminish~~ may reduce shear-driven turbulence~~relative to wave-driven contributions. Within this context, the observed decrease in La_t~~. Although these processes are not explicitly resolved at model resolution, the results indicate that wave forcing can remain dynamically relevant even at high SIC~~is interpreted as evidence for episodic wave influence under summer ice conditions, indicating that SIC alone~~. In this context, SIC provides a first-order constraint on mixing regimes, but does not uniquely ~~constrain the wave impact on upper-ocean~~ determine the relative importance of wave-driven turbulence during the melt season.

Panel (b) highlights the ~~local variability~~ role of local spatial variability by showing the distribution of La_t ~~using histograms of the minimum, mean, and maximum values computed over local~~ within 3×3 grid-cell neighborhoods. ~~These neighborhood diagnostics are introduced to characterize the local dynamical environment experienced by each MIZ grid cell. The minimum value,~~ The distributions of $La_t^{\min}$, ~~identifies~~ La_t^{mean}, and $La_t^{\max}$ demonstrate that a wide range of mixing states can coexist locally, even under similar SIC conditions. In particular, $La_t^{\min}$ captures the most wave-influenced ~~neighboring point and provides an upper bound on local wave impact~~conditions within a neighborhood, while $La_t^{\max}$ reflects the most shear-dominated ~~condition in the vicinity. The neighborhood mean, La_t^{mean}, closely tracks the single-grid-cell~~ state. The large spread between these values indicates strong heterogeneity in wave and shear forcing, consistent with a dynamic ice cover containing a mixture of wave-active and wave-suppressed regions. Panel (c) further quantifies this heterogeneity as the difference between local maximum and minimum La_t ~~, representing the dominant local regime, whereas the extremes reveal local scale variability that is masked by spatial averaging. Together, these distributions demonstrate that mixing regimes within the MIZ arise not only from seasonal modulation of SIC but also from strong~~ within each neighborhood. Heterogeneity increases from low SIC and peaks within the MIZ (SIC $\approx$ 0.3–0.5), reflecting the coexistence of wave- and shear-dominated regimes. At higher SIC, heterogeneity decreases, indicating a transition toward more spatially uniform forcing conditions. Overall, these show that while SIC governs the large-scale transition between mixing regimes, the realized La_t within a given SIC range depends strongly on local ice structure. Fragmentation and spatial heterogeneity in ~~wave and shear forcing at scales smaller than the model grid. This scale dependence suggests that conventional one-dimensional upper-ocean boundary layer parameterizations may inadequately represent mixing processes under partial ice cover, motivating the use of regime-based or local scale-aware approaches in ice–ocean models~~sea ice conditions modulate the intermittency of wave forcing, resulting in highly variable mixing conditions.

3.4 Pan-Arctic dissipation rates and seasonality

~~Figure 5 provides energetic context for the regime instability patterns identified in Figures 3–4 by explicitly characterizing both the magnitude and intermittency of mechanically driven upper-ocean dissipation under partial ice cover. Panel (a) shows~~

Mechanically driven dissipation provides a bulk measure of wind and wave energy input to the upper ocean and complements the regime-based analysis of LT. In our framework, $\varepsilon_{\text{mech}}$ quantifies the magnitude of mechanically mediated energy input, while La_t determines how this energy is partitioned between shear- and wave-driven processes. Figure 5a shows that the spatial distribution of median ~~mechanical dissipation over 2018–2022 for SIC $\geq$ 0.15. Persistent dissipation is concentrated along the marginal ice zone, wave-exposed shelves, and the seasonal ice edge, while the interior~~ $\varepsilon_{\text{mech}}$ is strongly structured by surface forcing, with enhanced dissipation along the MIZ and in peripheral seas exposed to open-ocean winds and wave activity. In contrast, the central pack ice exhibits ~~weak and spatially uniform dissipation~~lower dissipation, consistent with reduced momentum transfer and attenuated wave forcing beneath consolidated ice. This pattern reflects the ~~long-term background~~

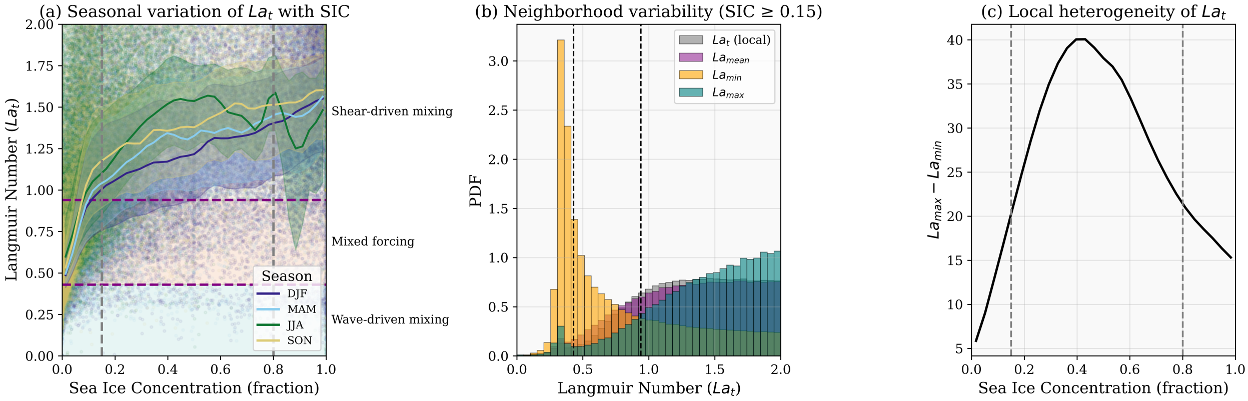

Figure 4. ~~**Sea ice concentration dependence of the turbulent Langmuir number.**~~ **Langmuir number dependence on sea ice concentration and spatial variability.** (~~**Left**~~**a**) Parametric ~~plot of La_t against~~ relationship between La_t and binned sea ice concentration (SIC). Solid lines denote the seasonal median ~~La_t for~~ within each ~~season and~~ SIC bin, with shading indicating ~~inter-quartile~~ interquartile ranges. ~~The white~~ Purple dashed lines mark the wave-dominated (~~$La_t < 0.43$~~$La_t < 0.43$) and shear-dominated (~~$La_t > 0.94$~~$La_t > 0.94$) regime thresholds. (~~**Right**~~**b**) Normalized ~~histogram~~ histograms of ~~La_t~~ La_t computed from local grid-cell values ~~in each smoothing category~~and 3×3 neighborhood statistics (mean, minimum, and maximum), aggregated over all ice-covered grid cells (~~$\mathrm{SIC} \geq 0.15$~~$\mathrm{SIC} \geq 0.15$). ~~This histogram highlights the asymmetry and variability~~ (**c**) Median local heterogeneity in ~~the spatial scale and intensity~~ La_t, defined as $La_{t,\max} - La_{t,\min}$ within 3×3 neighborhoods, as a function of ~~Langmuir turbulence across the Arctic~~SIC.

~~structure of mechanical~~ large-scale distribution of mechanically driven energy input and ~~identifies~~ highlights regions where wind–wave forcing recurrently couples to the upper ocean. Panel (b) ~~reveals a complementary aspect of the forcing environment by mapping~~ shows dissipation intermittency, ~~quantified as $log_1 0$ (P90/median).~~ defined as $\log_{10}(P_{90}/\mathrm{median})$ of $\varepsilon_{\mathrm{mech}}$, where the 90th percentile and median are computed from the temporal distribution at each grid cell. This metric quantifies the relative importance of extreme events compared to the background state. High intermittency is strongly localized to narrow MIZ regions and ~~ice edge~~ ice-edge corridors, indicating that dissipation in these areas is dominated by episodic events~~rather than sustained forcing~~. In contrast, regions with elevated median dissipation but low intermittency ~~experience comparatively steady~~ reflect more persistent, but still moderate, energy input. ~~The close~~

The spatial correspondence between highly intermittent dissipation and ~~previously identified~~ regime-transition hotspots ~~demonstrates~~ suggests that frequent mixing-regime changes arise ~~preferentially where competing~~ where wind-, wave-, and ice-mediated ~~processes~~ forcing alternately dominate on short timescales. ~~The~~ This link is further supported by the Arctic-wide time series in panel (c)~~further emphasizes the event-driven nature of mechanical dissipation, with variability dominated~~, which shows that variability in $\varepsilon_{\mathrm{mech}}$ is driven by intermittent extremes superimposed on a low median background. The large interquartile range relative to the median indicates that rare, high-energy events contribute disproportionately to temporal variability~~, consistent with the episodic forcing implied by the intermittency index. Panel~~. This indicates that mechanical dissipation in the Arctic is not controlled by the mean state, but by intermittent high-energy events that dominate variability.

Panel (d) shows that ~~this intermittency is seasonally modulated , with dissipation peaking during~~ dissipation is strongly modulated by season, with peaks in late summer and early autumn ~~when ice cover is thinning and wave penetration is enhanced, and reaching~~ and a minimum during late winter under consolidated ice. This seasonal cycle reflects the combined influence of increasing wind stress, reduced ice cover, and enhanced wave activity, all of which act to amplify mechanical energy input into the mixed layer. In the MIZ, mean forcing sets the spatial structure of dissipation, while intermittent events control its variability.

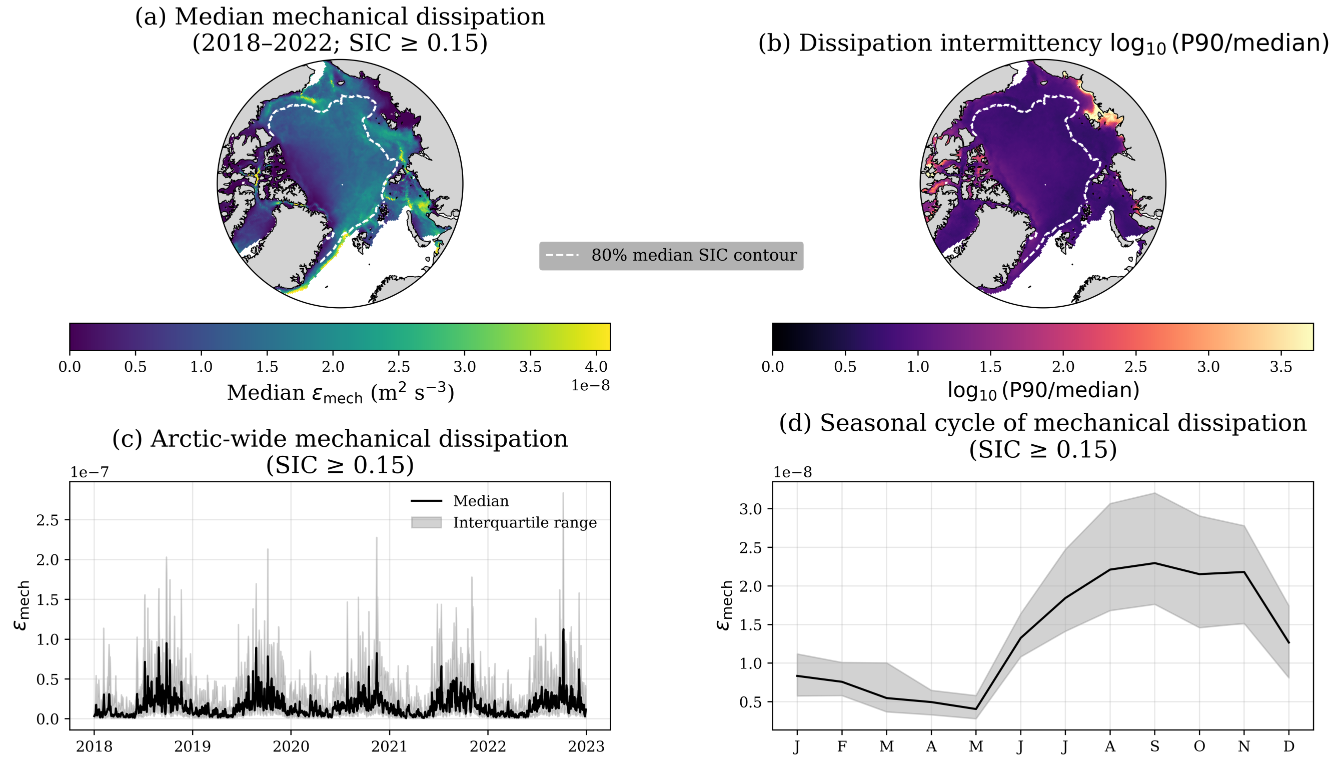

Figure 5. Mechanical dissipation magnitude and intermittency within the Arctic marginal ice zone (2018–2022). (a) Spatial distribution of the aggregated median mechanically forced dissipation, $\varepsilon_{\mathrm{mech}}$, evaluated for ice-covered conditions (SIC $\geq$ 0.15). **(b)** Dissipation intermittency index, defined as $\log_{10}(\mathrm{P90}/\mathrm{median})$ of $\varepsilon_{\mathrm{mech}}$. **(c)** Arctic-wide temporal evolution of mechanically forced dissipation aggregated over all grid cells classified as MIZ (SIC $\geq$ 0.15), shown as the spatial median (black line) with interquartile range (shading), illustrating the strongly intermittent nature of MIZ energy input. **(d)** Seasonal cycle of mechanically forced dissipation within the MIZ, constructed from the monthly climatology of the spatial median in panel (c), with shading indicating the interquartile range.

3.5 Impact of wind–wave misalignment on Langmuir turbulence efficiency

~~While Figure 5 demonstrates that mechanically driven dissipation in the MIZ is highly intermittent and dominated by episodic events, the extent to which~~ The contribution of wave-induced forcing ~~contributes to vertical mixing depends critically on~~ to

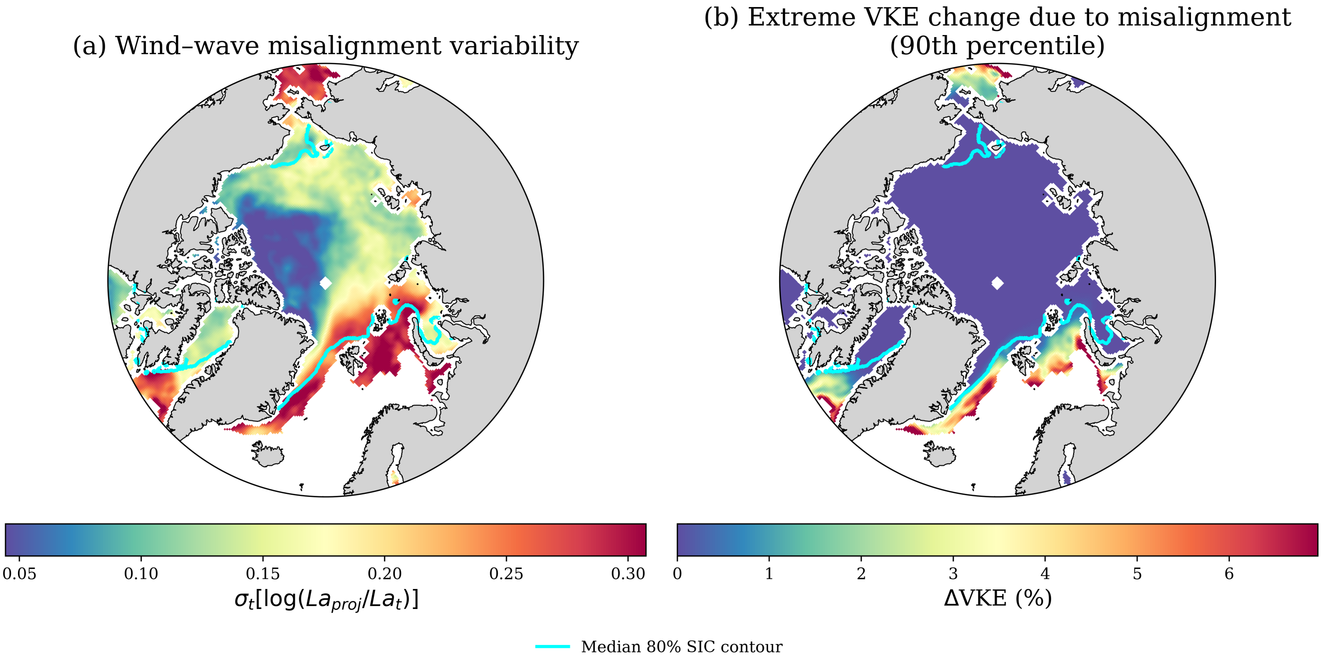

Figure 6. Impact of wind–wave misalignment on Langmuir turbulence across the Arctic. (a) Spatial variability of the projected-to-aligned Langmuir number ratio, expressed as the temporal standard deviation $\sigma_t[\log(La_{\mathrm{proj}}/La_t)]$, showing regions where wind–wave misalignment most strongly modulates LT diagnostics. (b) Corresponding impact of misalignment on LT energetics, shown as the 90th percentile change in normalized vertical kinetic energy (ΔVKE, %), indicating the upper bound of misalignment effects. The cyan contour denotes the median 80% sea ice concentration.

upper-ocean mixing depends not only on wave strength but also on the relative alignment ~~of~~ between wind and waves. To ~~isolate the role of wind–wave geometry in modulating Langmuir-driven mixing , we explicitly~~ quantify how directional misalignment modulates LT mixing potential, we compare wind-aligned and dynamically projected Langmuir ~~diagnostics using both local time series and pan-Arctic statistics. This analysis distinguishes between the *existence* of Langmuir forcing, as indicated by the turbulent Langmuir number La_t, and the *efficiency* with which that forcing is converted into vertical motions under realistic wind–wave alignment.~~

~~Because wind–wave misalignment is a local geometric property of the surface forcing rather than a spatially averaged quantity, all misalignment diagnostics are evaluated at the native model grid scale. Spatial smoothing does not qualitatively alter the inferred suppression of Langmuir-driven vertical motions, but it obscures the episodic nature of misalignment events and is therefore avoided here.~~

~~We first illustrate the impact of wind–wave misalignment using time series extracted at two dynamically contrasting locations representative of (i) the seasonal MIZ and (ii) the consolidated central Arctic (Figure 6) . For each site, we show~~ metrics across the Arctic. Misalignment variability is evaluated using the temporal standard deviation of the ~~standard La_t, the projected~~

~~Langmuir number accounting for dynamically oriented Langmuir cells (La_{proj}), the mixed-layer-averaged vertical velocity variance $\langle w'^2\rangle_{H_{\mathrm{ML}}}$ estimated from LES-based scalings, and daily sea ice concentration (SIC). Together, these metrics allow direct comparison between the potential for Langmuir forcing and its realized efficiency under evolving wind–wave alignment.~~

~~At the MIZsite, both La_t and La_{proj} exhibit pronounced seasonal variability associated with the expansion of the ice cover. Periods of reduced SIC permit wavepenetration and enhanced Stokes drift, leading to episodic transitions into mixed- and wave-driven forcing regimes. During these intervals, La_{proj} is frequently lower than La_t, reflecting geometric suppression of Langmuir forcing due to wind–wave misalignment. These misalignment events coincide with elevated VKE, indicating that LT is energetically active but occurs at reduced efficiency relative to a wind-aligned reference state. In contrast, periods of high SIC are characterized by weak VKE and little distinction between La_t and La_{proj}, consistent with strong wave attenuation beneath the ice cover.~~

~~The central Arctic site exhibits markedly different behavior. Persistently high SIC limits wave penetration throughout~~ log-ratio between projected and aligned Langmuir numbers, $\sigma_t[\log(La_{\mathrm{proj}}/La_t)]$, which captures fluctuations in the effective projection of Stokes forcing onto the Langmuir cell axis. Pan-Arctic spatial patterns (Figure 6a) show that variability in the projected-to-aligned Langmuir number ratio ranges from approximately 0.05 to 0.30, with the largest values confined to the MIZ, particularly in regions of persistent wave–ice interaction such as the Barents and Greenland Seas. In contrast, the central Arctic exhibits consistently low variability ($\lesssim 0.1$), reflecting weak wave forcing in compact ice cover. Despite this pronounced spatial variability in diagnostic LT metrics, the impact on LT energetics is limited. The 90th percentile change in VKE (Figure 6b) remains below $\sim 1\%$ across most of the ~~year, resulting in consistently large Langmuir numbers and weak VKE. Differences between La_t and La_{proj} are small and infrequent, indicating that wind–wave misalignment plays a secondary role where wave-induced~~ ice-covered Arctic and exceeds 4–6% only in localized regions near the ice edge. These regions correspond to partial ice cover and active wave propagation, where Stokes drift is ~~already strongly suppressed. Even when brief reductions in SIC occur, the associated misalignment produces only modest changes in VKE due to the overall lack of energetic wave forcing.~~ ~~**Impact of wind–wave misalignment on Langmuir turbulence at representative Arctic sites.**~~ ~~Time series extracted at a consolidated central Arctic location (**a,b**) and a seasonal MIZ location (**c,d**). Panels (**a**) and (**c**) show the Langmuir misalignment metric $\Delta La = La_{\mathrm{proj}} - La_t$, where La_t is the wind-aligned turbulent Langmuir number and La_{proj} accounts for dynamically projected Langmuir cell orientation. Negative values indicate geometric suppression of Langmuir forcing due to wind–wave misalignment. Sea ice concentration (SIC) is overlaid on a secondary axis (dashed teal line). Panels (**b**) and (**d**) show the mixed-layer-averaged vertical velocity variance $\langle w'^2\rangle_{H_{\mathrm{ML}}}$ estimated from LES-based scalings, comparing wind-aligned (blue) and projected (green) Langmuir forcing.~~ sufficiently strong for directional effects to influence the projected shear. These magnitudes indicate that although misalignment can significantly perturb diagnostic LT metrics, its effect on the resulting mixing is comparatively weak.

~~These local time series demonstrate that wind–wave misalignment does not determine whether LT is present, but rather modulates its efficiency when wave-driven forcing is active. Misalignment effects are therefore most pronounced in the MIZ, where partial ice cover allows wave penetration and energetic Langmuir motions, while they remain muted in the consolidated~~

~~central Arctic. This motivates a broader, pan-Arctic assessment of misalignment-driven suppression of LT efficiency, which we quantify below using a non dimensional efficiency metric.~~

~~**Geometric control of Langmuir turbulence efficiency by wind–wave misalignment.** (**a**) Dependence of the Langmuir efficiency factor $R_{LT} = \langle w'^2 \rangle_{La_{\mathrm{proj}}} / \langle w'^2 \rangle_{La_t}$ on the Langmuir cell orientation angle α_{LOW} for all ice-covered grid cells. Gray points show individual grid–time samples, while the black curve and shading denote the binned median and interquartile range. (**b**) Same data recast as a function of $\cos^2(\alpha_{\mathrm{LOW}})$, highlighting the underlying geometric control on Langmuir efficiency. Colored curves show regime-conditioned medians for shear-dominated, mixed-forcing, and wave-dominated regimes, with shaded envelopes indicating interquartile ranges. The dashed line denotes the ideal geometric scaling $R_{LT} = \cos^2 \alpha$.~~

~~To quantify the impact of wind–wave misalignment across the Arctic, we define the ratio~~

~~$R_{LT} = \langle w'^2 \rangle_{La_{\mathrm{proj}}} / \langle w'^2 \rangle_{La_t},$~~

~~which measures the efficiency of Langmuir-driven vertical motions relative to a wind-aligned reference state. Here, R_{LT} is interpreted as an efficiency factor: values near unity indicate that Langmuir-driven vertical motions approach their wind-aligned maximum, while lower values quantify the fraction of Langmuir potential lost due to wind–wave misalignment.~~

To assess how frequently wind–wave misalignment occurs and how it relates to LT variability, we examine the distribution of misalignment angles together with their co-occurrence with wave forcing and the resulting LT response (Figure 7). The angle distribution (Figure 7a~~shows that R_{LT} decreases systematically with increasing Langmuir cell orientation angle α_{LOW}, demonstrating a progressive suppression of VKE as wind–wave alignment deteriorates. R_{LT} approaches unity only under near-perfect alignment and does not exceed unity, confirming that Langmuir cell rotation acts as a purely geometric limiter rather than an amplifying mechanism. Across the MIZ, wind–wave misalignment typically reduces Langmuir-induced vertical velocity variance by 30–50% relative to wind-aligned estimates, with stronger suppression during shear-dominated conditions. Recasting the same relationship in terms of $\cos^2(\alpha_{\mathrm{LOW}})$ reveals a near-collapse of R_{LT} across shear-dominated, mixed-forcing, and wave-dominated regimes~~) shows that moderate-to-large misalignment is relatively common, with more than half of cases exceeding ∼30°. However, the joint distribution with wave strength (Figure 7b) ~~. In all regimes, Langmuir efficiency closely follows the ideal geometric scaling $R_{LT} = \cos^2 \alpha$, with regime-dependent offsets reflecting differences in baseline forcing rather than changes in functional behavior. This collapse demonstrates that wind–wave alignment primarily controls the *efficiency* with which Langmuir forcingis converted into vertical motions, while the underlying forcing regime governs the available Langmuir potential.~~

~~Across all MIZ grid cells ($0.15 \leq \mathrm{SIC} \leq 0.8$), the median value of R_{LT} is 0.84, with an interquartile range of 0.34–1.00, indicating that wind–wave misalignmentgenerally produces modest suppression of Langmuir-driven vertical velocity variance, while occasionally reducing it by more than 60% during strongly misaligned events. The full distribution of R_{LT} across the MIZ is shown in Supplemental Fig. S3~~indicates that these larger angles are most often associated with relatively weak wave forcing. ~~Wind–wave misalignment therefore emerges as a physically robust, regime-independent geometric modulator of Langmuir turbulence efficiency when wave-driven forcing is active in the Arctic, distinct from variations in the local wave–shear balance~~The energetic response remains small across all angles (Figure 7c), with changes in VKE close to zero

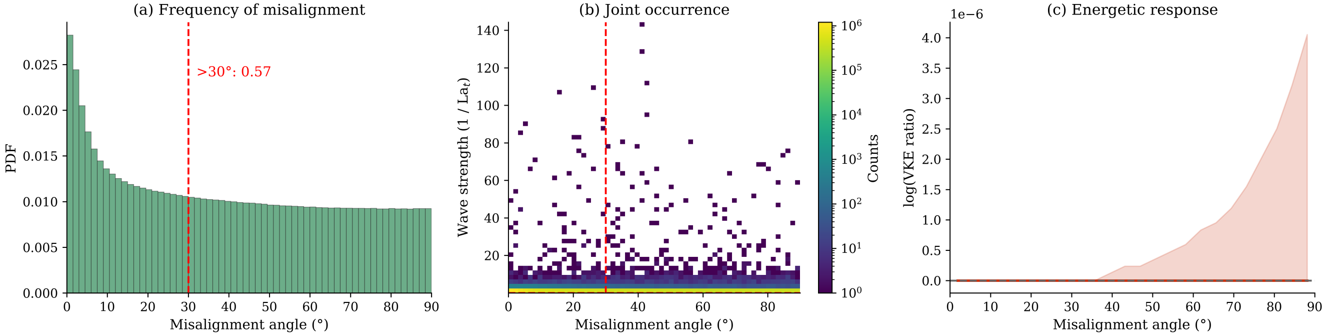

Figure 7. Frequency and impact of wind–wave misalignment on Langmuir turbulence (LT). (a) Probability density function (PDF) of wind–wave misalignment angles. A threshold of 30° is used to distinguish moderate misalignment, consistent with the distribution of angles shown in Figure7̃a. (b) Joint distribution of misalignment angle and wave strength (represented by $1/La_t$), showing the frequency of co-occurring conditions, with color indicating counts. The dashed line denotes the same 30°threshold. (c) Energetic response to misalignment, expressed as the median log-ratio of vertical kinetic energy (VKE) computed with and without directional effects, as a function of angle, with shading indicating the interquartile range (IQR)

in most cases and only limited variability at larger misalignment. These suggest that variability in projected LT metrics does not translate directly into changes in mixing, and that the influence of misalignment on LT is secondary compared to variations in wave forcing.

4 Discussion and Conclusions

4.1 ~~The marginal ice zone as a dynamically distinct mixing regime~~

~~Our results demonstrate that surface forcing capable of sustaining Langmuir turbulence (LT) in the Arctic is both spatially confined and temporally intermittent. Conditions resembling open-water wind–wave forcing occur predominantly within the seasonal marginal ice zone (MIZ)~~We used a coupled sea ice–wave modeling framework to quantify the controls on LT mixing potential across the Arctic basin. We show that LT-relevant forcing is fundamentally wave-limited, with Stokes drift strongly attenuated beneath sea ice despite frequent wind forcing of OW magnitude. Favorable conditions for LT mixing are intermittent and largely confined to the MIZ, while the interior pack ice remains ~~largely shear dominated. Even within~~ persistently shear-dominated. Mixing regimes showed clear spatial and temporal organization, with intermittent, event-driven transitions concentrated in the MIZ, ~~joint exceedance of wind stress and Stokes drift rarely exceeds 20% of the time,~~ superimposed on otherwise persistent seasonal states. We further demonstrate that SIC alone does not uniquely determine LT forcing, as local wave conditions and ice heterogeneity modulate the balance between shear- and wave-driven turbulence. Finally, we show that while wind–wave misalignment introduces substantial variability in diagnostic LT metrics, its impact on mixing remains small, indicating that LT ~~beneath ice is not a persistent background process but instead emerges episodically.~~ efficiency is controlled primarily by the magnitude of wave forcing rather than its orientation. This work provides a coherent framework for interpreting the spatial and temporal structure of LT mixing potential across the Arctic, highlighting the following key findings.

~~A pronounced seasonal asymmetry further characterizes this behavior. Despite the largest spatial extent of the MIZ during summer, LT-relevant forcing and Langmuir enhancement are weakest in this season. This counterintuitive result reflects the competing effects of ice retreat and waveattenuation: moderate ice concentrations efficiently damp Stokes drift, consistent with theoretical and observational studies documenting rapid decay of wave energy and Stokes transport under partial ice cover (Liu and Mollo-Christensen, 1988; Ardhuin et al., 2016; Herman, 2017), while summer winds tend to be weaker and less coherent~~

4.1 The marginal ice zone as a dynamically distinct mixing regime

The MIZ emerges not simply as a geometric transition zone, but as a dynamically distinct mixing regime in which wave, wind, and ice processes interact to produce intermittent LT forcing. While conditions resembling open-water forcing occur primarily within the MIZ, LT activity is not controlled by MIZ extent alone. Instead, it is governed by the intensity and coherence of wind–wave forcing, which varies seasonally and episodically. As a result, ~~expanded MIZ area does not translate into~~ periods of broad MIZ coverage do not necessarily correspond to enhanced LT activity, whereas dynamically active ice-edge regions can support strong, transient LT forcing.

~~In contrast, winter and transitional seasons exhibit more frequent and spatially coherent open-water–like forcingalong the evolving ice edge. During these periods, episodic storms generate strong winds and long-period swell that can temporarily overcome wave attenuation and penetrate into the MIZ (Thomson, 2022; Boutin et al., 2022). These events produce brief but dynamically significant excursions toward low La_t, enhanced mechanical dissipation, and elevated LT efficiency. Taken together, our results show that the seasonal imprint of LT in the Arctic is governed by the intensity and coherence of wind–wave forcing rather than by MIZ~~ The mixing regime-based analysis further shows that LT variability is closely linked to threshold behavior between shear-, mixed-, and wave-dominated states. Regime instability peaks where grid cells frequently cross these physically defined boundaries, indicating that mixing variability arises from fluctuations in forcing that shift the balance between competing processes, rather than from large-scale ice extent alone. This ~~finding is consistent with conceptual views of~~ highlights the MIZ as a ~~dynamically active wave–ice interactionzone rather than a purely geometric transition region (Squire and Williams, 2008; Horvat and Tziperman, 2015)~~region of enhanced variability and frequent reorganization of surface forcing, where LT emerges intermittently in response to episodic wave–ice interaction. This behavior extends earlier work showing that ice-edge variability is governed by dynamical thresholds rather than ice extent alone (Horvat et al., 2016).

4.2 Sea ice regulation of Stokes drift and Langmuir turbulence mixing potential~~Across all diagnostics, sea ice concentration (SIC) emerges as~~

SIC provides a first-order ~~regulator of~~ constraint on the *mean* balance between wave- and shear-driven turbulence by regulating the attenuation of Stokes drift. For most seasons, median La_t increases ~~monotonically~~ with SIC, reflecting the progressive suppression of ~~Stokes drift~~ wave-driven forcing relative to wind stress as ice cover increases. ~~Consequently,~~ This leads to predominantly shear-dominated conditions in the central Arctic~~is characterized by persistently shear-dominated conditions, long regime persistence, and weak variability in LT-related metrics.~~

~~Departures from this monotonic relationship during summer, most notably~~. However, SIC alone does not fully explain the variability in LT forcing. Significant departures from the mean SIC–La_t relationship arise across seasons, indicating that additional processes modulate the realized balance between wave and shear forcing. In particular, reduced La_t at higher SIC ~~, do not indicate sustained wave forcing within the interior pack. Instead, they reflect~~ during summer reflects intermittent wave penetration enabled by thinner, more fragmented ice and enhanced floe-scale heterogeneity~~during the melt season~~. Under these conditions, long-period swell can episodically access ~~regions that remain nominally ice covered, temporarily reducing La_t without establishing a persistent~~ nominally ice-covered regions, temporarily enhancing Stokes drift without establishing sustained wave-driven ~~regime. These results highlight that while SIC controls~~ mixing. This indicates that SIC constrains the background forcing state ~~, the mechanical properties of the ice and the spectral characteristics of the wave field modulate the realization of wave influence in ways not captured by concentration alone.~~ but does not capture the processes that govern LT variability and intermittency.

4.3 ~~Forcing intermittency, regime instability, and Langmuir efficiency~~

~~The regime-based analysis further reveals that the MIZ is not merely a spatial transition zone but a dynamically distinct environment characterized by enhanced variability and frequent reorganization of surface forcing. Regime instability peaks when grid cells reside near thresholds separating shear-, mixed-, and wave-dominated regimes, rather than when the MIZ is most extensive. Periods of broad MIZ coverage are often dynamically stable, whereas narrow, rapidly evolving ice edges promote frequent regime switching. This behavior extends earlier work showing that ice-edge variability is governed by dynamical thresholds rather than ice extent alone (Horvat et al., 2016).~~

~~Energetic diagnostics indicate that this instability is driven~~

4.3 Energetics and the role of misalignment

Energetic metrics show that variability in LT mixing is governed primarily by the intermittency of mechanical ~~dissipation rather than by~~ forcing rather than its mean magnitude. Highly intermittent dissipation is strongly localized to the same MIZ corridors that exhibit frequent regime transitions, ~~demonstrating that episodic forcing eventsassociated with storms and wave penetration dominate the dynamical evolution of the system. This finding aligns with broader evidence~~ indicating that episodic events, such as storms and transient wave penetration, dominate the temporal evolution of mixing. This behavior is consistent with previous studies showing that turbulent mixing in both open-ocean and ice-covered environments is controlled by intermittent, high-energy events rather than by time-mean forcing (Belcher et al., 2012; McWilliams, 2016; Ardhuin et al., 2016; Thomson, 2022; Boutin et al., 2022).

~~Explicitly accounting for wind–wave misalignment further refines the diagnosis of Langmuir-driven mixing. Comparisons between wind-aligned and dynamically projected Langmuir diagnostics show that misalignment acts as a systematic~~ Wind–wave misalignment introduces an additional geometric constraint on LT efficiency by reducing the effective ~~Stokes shear projected~~ projection of Stokes shear onto the Langmuir cell axis. ~~This behavior is consistent with theoretical and large-eddy simulation studies demonstrating that Langmuir turbulence intensity depends not only on the magnitude of Stokes drift but also on its orientation relative to the wind stress (McWilliams et al., 1997; Harcourt and D'Asaro, 2008; Harcourt, 2015; Van Roekel et al., 2012). Increasing misalignment suppresses vertical velocity variance even when wave forcing is present.~~ While spatial diagnostics indicate substantial variability in projected LT metrics, the statistical analysis of misalignment angles shows that near-aligned conditions dominate, with most angles below ∼20°, and larger misalignment occurring primarily in the MIZ. Consistent with this, the energetic response to misalignment is weak. Hence, despite misalignment perturbing LT metrics, its effect on mixing is secondary,with typical changes in VKE remaining small relative to variability driven by wave forcing. LT energetics are controlled primarily by the magnitude and intermittency of wave forcing, while geometric effects act only as a weak modulation. In summary, LT in the Arctic is primarily controlled by intermittent wave forcing within the MIZ, with sea ice setting the background state and misalignment playing a secondary role.

~~In our analysis, wind–wave misalignment reduces the realized contribution of LT to vertical mixing across all surface forcingregimes without altering the underlying regime classification. Thus, while La_t determines whether Langmuir forcingis present, geometric alignment governs how efficiently that forcing is converted into vertical motions. Together, our results demonstrate~~

4.4 Implications for Arctic mixed layer dynamics and model development

Our results show that LT in the Arctic is ~~highly heterogeneous in space and time, responding dynamically to variations in waves,~~ strongly constrained by wave–ice interactions. Wave attenuation beneath consolidated ice limits Stokes drift and confines wave-driven mixing primarily to the MIZ. Thus, parameterizations based on open-ocean conditions are likely to overestimate both the extent and persistence of Langmuir-driven mixing in ice-covered regions. LT forcing is also highly intermittent, driven by episodic wind–wave events along the evolving ice edge. Capturing this variability requires parameterizations that respond to changes in Stokes drift, rather than relying solely on bulk ice properties or steady forcing assumptions. In contrast, wind–wave misalignment plays a secondary role. Although it modifies diagnostic LT metrics, its effect on energetics is small relative to variability associated with wave forcing. These results suggest that improving the representation of wave attenuation and Stokes drift under sea ice ~~, and windgeometry. The MIZ emerges as the primary region where intermittent forcing, geometric constraints, and competing production mechanisms interact, underscoring the need for regime-aware and geometry-aware representations of upper-ocean mixing under partial ice cover~~is more important than explicitly resolving directional effects for modeling Arctic mixed-layer dynamics.

4.5 Limitations and ~~Future Directions~~future directions

Our approach is based on bulk diagnostics and empirically derived scalings and therefore carries several important limitations. The use of ∼25 km resolution fields limits our ability to resolve fine-scale processes such as ~~mesoscale and~~ submesoscale eddies, floe-scale wave attenuation, and narrow leads and polynyas, all of which can locally modulate ~~Langmuir turbulence~~ LT and upper-ocean mixing. ~~Although~~ While neighborhood-based statistics partially capture local heterogeneity, direct assessment of ~~small-scale Langmuir dynamics ultimately~~ these processes requires higher-resolution modeling and targeted *in situ* observations.

In addition, our analysis relies on a coupled sea ice–wave framework in which the ocean mixed layer does not respond dynamically to wind–wave forcing~~and explicit ocean~~ , and stratification feedbacks are not explicitly resolved. Mixed-layer depth and buoyancy effects are ~~therefore prescribedrather than prognostic, constraining~~ prescribed, limiting the realism of the diagnosed vertical mixing response. In particular, buoyancy-driven convection and ~~Langmuir turbulence~~ LT are expected to interact nonlinearly in ice-covered and meltwater-influenced environments, yet their relative contributions remain poorly constrained~~in the present framework~~. As a result, the ~~diagnostics~~ metrics presented here should be interpreted as indicators of ~~Langmuir~~ LT mixing *potential*~~rather than as~~ , rather than predictions of realized turbulent states.

4.5.1 ~~Implications for ocean and climate modeling.~~

~~Despite these limitations, our results provide several clear implications for the representation of upper-ocean mixing under partial ice cover in climate and Earth system models. First, the strong intermittency and regime dependence of Langmuir turbulence in the MIZ imply that parameterizations based on time-mean forcing or sea ice concentration alone are unlikely to capture the episodic nature of mechanically driven mixing. Instead, regime-aware formulations that respond to joint wind–wave conditions and their temporal variability are required.~~

~~Second, our analysis demonstrates that wind–wave misalignment acts as a systematic geometric limiter on LT efficiency, independent of the underlying wave–shear balance. This finding suggests that existing Langmuir parameterizations, which often assume wind-aligned Stokes drift, may systematically overestimate vertical mixing in partially ice-covered regions unless geometric effects are explicitly accounted for. Incorporating misalignment-aware scaling factors or projected Stokes drift formulations offers a physically grounded pathway for improving LT representations without substantially increasing model complexity.~~

~~Finally, the spatial confinement of LT-relevant forcing to narrow, evolving MIZ corridors highlights the need for parameterizations that are robust across sharp transitions in surface state. In coarse-resolution models, where the MIZ is often poorly resolved, neglecting this spatial and temporal localization may lead to either excessive mixing within the interior pack or insufficient mixing near the ice edge. Our results therefore motivate the development of scale-aware and regime-based mixing schemes that adapt dynamically to ice concentration, wave exposure, and wind–wave geometry.~~

Addressing these challenges ultimately requires fully coupled ocean–wave–ice models that resolve stratification, wave propagation beneath ice, and wind–wave misalignment simultaneously. Recent and ongoing studies are beginning to resolve Langmuir turbulence under partially ice-covered and weakly stratified regimes using large-eddy simulations, regional modeling, and coordinated observations (e.g., Brenner et al., 2023; Lee et al., 2025). These efforts provide a clear pathway toward stratification-aware, ice-modified Langmuir parameterizations.

Complementary observational efforts are also essential. Coordinated field campaigns employing autonomous profilers, SWIFT drifters, and satellite altimetry will be critical for evaluating Langmuir diagnostics and parameterizations in ice-covered waters. In particular, observational and modeling studies should prioritize the MIZ, where wave–ice–wind interactions are most dynamically active. Finally, quantifying the impact of ~~Langmuir turbulence~~ LT on vertical tracer transport, stratification erosion, and ice–ocean heat exchange in climate models will be essential for assessing its broader role in the evolving Arctic system.

. The model outputs and post-processed Langmuir turbulence diagnostics used in this study are publicly available via Zenodo at https://zenodo.org/records/17372007 and via the Arctic Data Center urn:uuid:566584ac-4d50-4641-9085-103a6728b8a0. Analysis scripts are hosted on GitHub at https://github.com/atavri/Langmuir_turbulence_Arctic.git. ERA5 atmospheric reanalysis data are available from the Copernicus Climate Data Store, and the GLORYS12V1 ocean reanalysis is available through the Copernicus Marine Service.

. A.T. led the study, including conceptualization, analysis, and writing of the original draft. C.H., B.P., and A.T. contributed to interpretation of results and manuscript review and editing. G.B. contributed to model data curation and technical support. A.H. and A.K. contributed to early analysis and scientific discussion.

. The authors declare that they have no competing interests.

. This research was supported in part by the National Science Foundation (NSF OPP-2146910 and OCE-2148655) and by Schmidt Sciences, LLC through the SASIP project. The simulations were performed using resources provided by Sigma2—the National Infrastructure for High-Performance Computing and Data Storage in Norway.

We thank Sam Brenner and Baylor Fox-Kemper for their assistance during the project initialization phase and for insightful discussions that helped shape the use of the Langmuir turbulence parameterizations.

References

Ali, A., Christensen, K. H., Breivik, Ø., Malila, M., Raj, R. P., Bertino, L., Chassignet, E. P., and Bakhoday-Paskyabi, M.: A comparison of Langmuir turbulence parameterizations and key wave effects in a numerical model of the North Atlantic and Arctic Oceans, Ocean Modelling, 137, 76–97, 2019.

Ardhuin, F., Sutherland, P., Doble, M., and Wadhams, P.: Ocean waves across the Arctic: Attenuation due to dissipation dominates over scattering for periods longer than 19 s, Geophysical Research Letters, 43, 5775–5783, 2016.

Ardhuin, F., Boutin, G., Stopa, J., Girard-Ardhuin, F., Melsheimer, C., Thomson, J., Kohout, A., Doble, M., and Wadhams, P.: Wave attenuation through an Arctic marginal ice zone on 12 October 2015: 2. Numerical modeling of waves and associated ice breakup, Journal of Geophysical Research: Oceans, 123, 5652–5668, 2018.

Ardhuin, F., Otero, M., Merrifield, S., Grouazel, A., and Terrill, E.: Ice breakup controls dissipation of wind waves across southern ocean sea ice, Geophysical Research Letters, 47, e2020GL087 699, 2020.

Armitage, T. W., Bacon, S., Ridout, A. L., Petty, A. A., Wolbach, S., and Tsamados, M.: Arctic Ocean surface geostrophic circulation 2003–2014, The Cryosphere, 11, 1767–1780, 2017.

Belcher, S. E., Grant, A. L., Hanley, K. E., Fox-Kemper, B., Van Roekel, L., Sullivan, P. P., Large, W. G., Brown, A., Hines, A., Calvert, D., et al.: A global perspective on Langmuir turbulence in the ocean surface boundary layer, Geophysical Research Letters, 39, 2012.

Boutin, G., Ardhuin, F., Dumont, D., Sévigny, C., Girard-Ardhuin, F., and Accensi, M.: Floe size effect on wave-ice interactions: Possible effects, implementation in wave model, and evaluation, Journal of Geophysical Research: Oceans, 123, 4779–4805, 2018.

Boutin, G., Lique, C., Ardhuin, F., Rousset, C., Talandier, C., Accensi, M., and Girard-Ardhuin, F.: Towards a coupled model to investigate wave–sea ice interactions in the Arctic marginal ice zone, The Cryosphere, 14, 709–735, 2020.

Boutin, G., Williams, T., Rampal, P., Olason, E., and Lique, C.: Wave–sea-ice interactions in a brittle rheological framework, Cryosphere, 15, 431–457, 2021.

Boutin, G., Williams, T., Horvat, C., and Brodeau, L.: Modelling the Arctic wave-affected marginal ice zone: a comparison with ICESat-2 observations, Philosophical Transactions of the Royal Society A, 380, 20210 262, 2022.

Brenner, S. and Horvat, C.: Scaling simulations of local wind-waves amid sea ice floes, Journal of Geophysical Research: Oceans, 129, e2024JC021 629, 2024.

Brenner, S., Rainville, L., Thomson, J., Cole, S., and Lee, C.: Comparing observations and parameterizations of ice-ocean drag through an annual cycle across the Beaufort Sea, Journal of Geophysical Research: Oceans, 126, e2020JC016 977, 2021.

Brenner, S., Horvat, C., Hall, P., Lo Piccolo, A., Fox-Kemper, B., Labbé, S., and Dansereau, V.: Scale-dependent air-sea exchange in the polar oceans: Floe-floe and floe-flow coupling in the generation of ice-ocean boundary layer turbulence, Geophysical Research Letters, 50, e2023GL105 703, 2023.

Collins, C., Doble, M., Lund, B., and Smith, M.: Observations of surface wave dispersion in the marginal ice zone, Journal of Geophysical Research: Oceans, 123, 3336–3354, 2018.

Cooper, V. T., Roach, L., Thomson, J., Brenner, S., Smith, M., Meylan, M., and Bitz, C.: Wind waves in sea ice of the western Arctic and a global coupled wave-ice model, Philosophical Transactions of the Royal Society A, 380, 20210 258, 2022.

Craik, A. D. and Leibovich, S.: A rational model for Langmuir circulations, Journal of Fluid Mechanics, 73, 401–426, 1976.

D'Asaro, E. A.: Turbulence in the upper-ocean mixed layer, Annual review of marine science, 6, 101–115, 2014.

Dethleff, D. and Kempema, E.: Langmuir circulation driving sediment entrainment into newly formed ice: Tank experiment results with application to nature (Lake Hattie, United States; Kara Sea, Siberia), Journal of Geophysical Research: Oceans, 112, 2007.

Dosser, H. V. and Rainville, L.: Dynamics of the changing near-inertial internal wave field in the Arctic Ocean, Journal of Physical Oceanography, 46, 395–415, 2016.

Drucker, R., Martin, S., and Moritz, R.: Observations of ice thickness and frazil ice in the St. Lawrence Island polynya from satellite imagery, upward looking sonar, and salinity/temperature moorings, Journal of Geophysical Research: Oceans, 108, 2003.

Fan, Y. and Griffies, S. M.: Impacts of parameterized Langmuir turbulence and nonbreaking wave mixing in global climate simulations, Journal of Climate, 27, 4752–4775, 2014.

Gargett, A. and Grosch, C.: Turbulence process domination under the combined forcings of wind stress, the Langmuir vortex force, and surface cooling, Journal of Physical Oceanography, 44, 44–67, 2014.

Harcourt, R. R.: An improved second-moment closure model of Langmuir turbulence, Journal of Physical Oceanography, 45, 84–103, 2015.

Harcourt, R. R. and D'Asaro, E. A.: Large-eddy simulation of Langmuir turbulence in pure wind seas, Journal of Physical Oceanography, 38, 1542–1562, 2008.

Herman, A.: Wave-induced stress and breaking of sea ice in a coupled hydrodynamic discrete-element wave–ice model, The Cryosphere, 11, 2711–2725, 2017.

Horvat, C. and Tziperman, E.: A prognostic model of the sea-ice floe size and thickness distribution, The Cryosphere, 9, 2119–2134, 2015.

Horvat, C., Tziperman, E., and Campin, J.-M.: Interaction of sea ice floe size, ocean eddies, and sea ice melting, Geophysical Research Letters, 43, 8083–8090, 2016.

Horvat, C., Blanchard-Wrigglesworth, E., and Petty, A.: Observing waves in sea ice with ICESat-2, Geophysical Research Letters, 47, e2020GL087 629, 2020.

Kirillov, S. A., Dmitrenko, I. A., Hölemann, J. A., Kassens, H., and Bloshkina, E.: The penetrative mixing in the Laptev Sea coastal polynya pycnocline layer, Continental Shelf Research, 63, 34–42, 2013.

Kukulka, T., Plueddemann, A. J., Trowbridge, J. H., and Sullivan, P. P.: Rapid mixed layer deepening by the combination of Langmuir and shear instabilities: A case study, Journal of Physical Oceanography, 40, 2381–2400, 2010.

Kukulka, T., Plueddemann, A. J., and Sullivan, P. P.: Inhibited upper ocean restratification in nonequilibrium swell conditions, Geophysical Research Letters, 40, 3672–3676, 2013.

Lee, A., Hutchings, J., Horvat, C., Tavri, A., and Pearson, B.: Impact of Surface Waves on Mixing and Circulation in a Summertime Lead, EGUsphere, 2025, 1–33, 2025.

Leibovich, S.: The form and dynamics of Langmuir circulations, Annual review of fluid mechanics, 15, 391–427, 1983.

Li, Q. and Fox-Kemper, B.: Assessing the effects of Langmuir turbulence on the entrainment buoyancy flux in the ocean surface boundary layer, Journal of Physical Oceanography, 47, 2863–2886, 2017.

Li, Q., Webb, A., Fox-Kemper, B., Craig, A., Danabasoglu, G., Large, W. G., and Vertenstein, M.: Langmuir mixing effects on global climate: WAVEWATCH III in CESM, Ocean Modelling, 103, 145–160, 2016.

Li, Q., Fox-Kemper, B., Breivik, Ø., and Webb, A.: Statistical models of global Langmuir mixing, Ocean Modelling, 113, 95–114, 2017.

Li, Q., Reichl, B. G., Fox-Kemper, B., Adcroft, A. J., Belcher, S. E., Danabasoglu, G., Grant, A. L., Griffies, S. M., Hallberg, R., Hara, T., et al.: Comparing ocean surface boundary vertical mixing schemes including Langmuir turbulence, Journal of Advances in Modeling Earth Systems, 11, 3545–3592, 2019.

Liu, A. K. and Mollo-Christensen, E.: Wave propagation in a solid ice pack, Journal of physical oceanography, 18, 1702–1712, 1988.

Lo Piccolo, A., Horvat, C., and Fox-Kemper, B.: Energetics and Transfer of Submesoscale Brine-Driven Eddies at a Sea Ice Edge, Journal of Physical Oceanography, 54, 1489–1501, 2024.

Manucharyan, G. E. and Thompson, A. F.: Submesoscale sea ice-ocean interactions in marginal ice zones, Journal of Geophysical Research: Oceans, 122, 9455–9475, 2017.

McWilliams, J. C.: Submesoscale currents in the ocean, Proceedings of the Royal Society A: Mathematical, Physical and Engineering Sciences, 472, 20160 117, 2016.

McWilliams, J. C. and Sullivan, P. P.: Vertical mixing by Langmuir circulations, Spill Science & Technology Bulletin, 6, 225–237, 2000.

McWilliams, J. C., Sullivan, P. P., and Moeng, C.-H.: Langmuir turbulence in the ocean, Journal of Fluid Mechanics, 334, 1–30, 1997.

Morison, J. H., Long, C. E., and Levine, M. D.: Internal wave dissipation under sea ice, Journal of Geophysical Research: Oceans, 90, 11 959–11 966, 1985.

Muilwijk, M., Hattermann, T., Martin, T., and Granskog, M. A.: Future sea ice weakening amplifies wind-driven trends in surface stress and Arctic Ocean spin-up, Nature Communications, 15, 6889, 2024.

Ólason, E., Boutin, G., Williams, T., Korosov, A., Regan, H., Rheinlænder, J., Rampal, P., Flocco, D., Samaké, A., Davy, R., et al.: The next generation sea-ice model neXtSIM, version 2, EGUsphere, 2025, 1–33, 2025.

Pearson, B. C., Grant, A. L., Polton, J. A., and Belcher, S. E.: Langmuir turbulence and surface heating in the ocean surface boundary layer, Journal of Physical Oceanography, 45, 2897–2911, 2015.

Pearson, B. C., Grant, A. L., and Polton, J. A.: Pressure–strain terms in Langmuir turbulence, Journal of Fluid Mechanics, 880, 5–31, 2019.

Pinkel, R.: Near-inertial wave propagation in the western Arctic, Journal of physical oceanography, 35, 645–665, 2005.

Polton, J. A. and Belcher, S. E.: Langmuir turbulence and deeply penetrating jets in an unstratified mixed layer, Journal of Geophysical Research: Oceans, 112, 2007.

Rainville, L., Lee, C. M., and Woodgate, R. A.: Impact of wind-driven mixing in the Arctic Ocean, Oceanography, 24, 136–145, 2011.

Rampal, P., Bouillon, S., Ólason, E., and Morlighem, M.: neXtSIM: a new Lagrangian sea ice model, The Cryosphere, 10, 1055–1073, 2016.

Reichl, B. G. and Li, Q.: A parameterization with a constrained potential energy conversion rate of vertical mixing due to Langmuir turbulence, Journal of Physical Oceanography, 49, 2935–2959, 2019.

Reichl, B. G., Wang, D., Hara, T., Ginis, I., and Kukulka, T.: Langmuir turbulence parameterization in tropical cyclone conditions, Journal of Physical Oceanography, 46, 863–886, 2016.

Skyllingstad, E. D. and Denbo, D. W.: An ocean large-eddy simulation of Langmuir circulations and convection in the surface mixed layer, Journal of Geophysical Research: Oceans, 100, 8501–8522, 1995.

Skyllingstad, E. D. and Denbo, D. W.: Turbulence beneath sea ice and leads: A coupled sea ice/large-eddy simulation study, Journal of Geophysical Research: Oceans, 106, 2477–2497, 2001.

Smyth, W. D., Skyllingstad, E. D., Crawford, G. B., and Wijesekera, H.: Nonlocal fluxes and Stokes drift effects in the K-profile parameterization, Ocean Dynamics, 52, 104–115, 2002.

Squire, V. and Williams, T.: Wave propagation across sea-ice thickness changes, Ocean Modelling, 21, 1–11, 2008.

Squire, V. A.: A fresh look at how ocean waves and sea ice interact, Philosophical Transactions of the Royal Society A: Mathematical, Physical and Engineering Sciences, 376, 20170 342, 2018.

Stopa, J. E., Ardhuin, F., and Girard-Ardhuin, F.: Wave climate in the Arctic 1992–2014: Seasonality and trends, The Cryosphere, 10, 1605–1629, 2016.

Sullivan, P. P., McWILLIAMS, J. C., and Melville, W. K.: Surface gravity wave effects in the oceanic boundary layer: Large-eddy simulation with vortex force and stochastic breakers, Journal of Fluid Mechanics, 593, 405–452, 2007.

Thomson, J.: Wave propagation in the marginal ice zone: connections and feedback mechanisms within the air–ice–ocean system, Philosophical Transactions of the Royal Society A, 380, 20210 251, 2022.

Thomson, J. and Rogers, W. E.: Swell and sea in the emerging Arctic Ocean, Geophysical Research Letters, 41, 3136–3140, 2014.

Tolman, H. L. et al.: User manual and system documentation of WAVEWATCH III TM version 3.14, Technical note, MMAB contribution, 276, 2009.

Van Roekel, L., Fox-Kemper, B., Sullivan, P., Hamlington, P., and Haney, S.: The form and orientation of Langmuir cells for misaligned winds and waves, Journal of Geophysical Research: Oceans, 117, 2012.

Voermans, J., Babanin, A., Thomson, J., Smith, M., and Shen, H.: Wave attenuation by sea ice turbulence, Geophysical Research Letters, 46, 6796–6803, 2019.

Webb, A. and Fox-Kemper, B.: Wave spectral moments and Stokes drift estimation, Ocean modelling, 40, 273–288, 2011.

Yang, D., Chamecki, M., and Meneveau, C.: Inhibition of oil plume dilution in Langmuir ocean circulation, Geophysical Research Letters, 41, 1632–1638, 2014.